APPLICATIONS OF INTRAVITAL NONLINEAR MICROSCOPY IN CARDIOVASCULAR RESEARCH

A Dissertation

Presented to the Faculty of the Graduate School

of Cornell University

In Partial Fulfillment of the Requirements for the Degree of

Doctor of Philosophy

by

Jason S. Jones

December 2018

APPLICATIONS OF INTRAVITAL NONLINEAR MICROSCOPY IN CARDOVASCULAR RESEARCH

Jason S. Jones, Ph.D.

Cornell University 2018

Coordinated contraction of the heart allows for efficient pumping of blood to the body, supplying organs with oxygen necessary for metabolism. In heart disease, reduction of blood flow to heart muscle tissue can result in damage to the tissue over time. The adult heart, unlike other organs, has a limited capacity to recover from this damage causing the mechanical work the heart can perform to decline over time. While our ability to restore flow to the heart and mitigate abnormal electrically conducting tissue has improved over the last few decades, therapies which restore mechanical function improving cardiac output, through repair and healing of the cardiac muscle have not been realized in the clinic.

Historic models used to study heart disease lack the ability to quantitative study the progression of individual cells within the living heart following an injury. Here I have taken some first steps in providing imaging methods and tools to allow the study of a more complete picture of heart disease in the context of the whole animal using multiphoton microscopy. I present methods for quantification of cellular resolved excitation and contraction, demonstrate the potential of THG as a label free signal to study the atherosclerotic plaque environment, and characterize some of the optical properties of the heart necessary to push the imaging depth accessible with current multiphoton technology.

BIOGRAPHICAL SKETCH

Jason Jones was born and raised in Stroudsburg, Pennsylvania. Jason attended Kutztown University of Pennsylvania where he entered as an undeclared major and finished double majoring in Physics and Mathematics. He began his research career during his final semester of undergrad under Dr. Perry Lee in the department of Mathematics modeling light propagation in tissue. He came to Cornell as a Masters of Engineering student in Biomedical Engineering and took on a proof of concept project aimed at taking the first cell resolved images of the beating heart in vivo using multiphoton microscopy. With initial success Jason chose to stay in the lab and continue this work on cardiac imaging as a PhD student where he focused on further developing the methods using more advanced microscopy. Following his graduate studies he plans to take an industrial position with KLA-Tencor working as a product development engineer, to continue working on advanced imaging systems.

For the Adirondacks,

may they always remain a sanctuary

ACKNOWLEDGMENTS

Cornell is an awe-inspiring place that brings people from so many cultures and backgrounds together in the name of higher education. It has been a truly humbling experience to be surrounded by so many great minds and personalities and has allowed me to grow in ways I'd never dreamed of. The PhD was a long and bumpy road filled with countless nights stranded in the sunless abyss that is the Weill hall basement and I would have never found my way out without the beautiful community that resides there. First and foremost I would like to thank my fellow hallway office dwellers, Mitch Pender who was there before we had the ability to turn the lights off at night (to sleep better in the office), Jeff Mulligan for his persistent optimism and dedication as an educator, Dr. John Foo for always finding an underlying lesson in every failed experiment, and Mohammad Haft for keeping the keyboards running like well oiled machines. Big thanks to Dr. David Small aka Mr. Postdoc, MVP of team cardiac, surgical wizard, and avid crossfitter, nothing would have ever worked without him. My committee members, Dr. Chris Xu and Dr. Michael Kotlikoff for their wisdom and insight that helped guide me at critical points during my graduate career. Thanks to undergrads Saif Azam and Sophia Hu for being a source of inspiration, Dr. Liz Wayne for her late night conversations as I was ushered into the exciting new world of academia, Dr. Oliver Bracko for having a wealth of mountain knowledge, Yuting Cheng for being Yu-ting, and Menansili Mejooli for being a great friend in lab and sacrificing a goat in my honor. Thanks to collaborators Dr. Frank Lee, Dr. Dimitre Ouzounov, and Dr. David Huland for teaching me tons and being great people.

In addition to growing as a researcher, Cornell allowed me to grow in many equally important ways, notably some of the people who contributed to this extra curricular growth are David Katz, who organized an expedition to Madagascar, showing me how much can be achieved through proper planning and risk

management, Chris Pelzer and Dr. Peter Lo who served as my whitewater kayaking mentors and pushed my abilities to levels I would have never though achievable, and my traveling companions Dr. Jean Carlos, Dr. Kirk Samaroo, Dr. Jose Rios, and Thong Cao who I have shared countless nights sleeping in tents, huts, hostels, boats and on airport floors in search of a broader understanding of the diverse world we find ourselves in.

My heart felt thanks to the residents of 203 Prospect St., Dr. Derek Holyoak, Dr. Ben Richards, Dr. Ben Cohen, Dr. Jason Guss, and Becka Irwin who created a beautiful home to come home to after a long day in lab and always had a project waiting ranging from putting engines together in the dinning room, crafting up the next entrepreneurial endeavor, making a craft beer, or serving as a part time therapist. A shout out to Nathan Ellis, manager of the graduate LASSP machine shop, possibly the only person on campus who had heard of the town my parents were from, without him there would have been a lot of crooked microscope parts stuck together, couldn't have got through without him. Thanks to my mother and late father who taught me to be strong and steadfast from the beginning. And of course last but not least to Chris and Nozomi for their continual loan of high end backpacking gear, sponsorship of lab outings, and occasional scientific guidance.

TABLE OF CONTENTS

LIST OF FIGURES

LIST OF ABBREVIATIONS

2PE	Two photon excitation
2PEF	Two photon excited fluorescence
3PE	Three photon excitation
ApoE	Apolipoprotein E gene
AutoF	Autofluorescence
CAL	Characteristic attenuation length
CARS	Coherent anti-Stokes Raman
CD68	Cluster of differentiation 68
DAPI	4′,6-diamidino-2-phenylindole
ECG	Electrocardiogram
FITC	Fluorescein isothiocyanate
FOV	Field of view
FPS	Frames per second
FWHM	Full width half maximum
Galvo	Galvanometric
GFP	Green fluorescent protein
GRIN	Gradient index of refraction
H&E	Hematoxylin and eosin
HF	High fat
IVUS	Intravascular ultrasound
MPM	Multiphoton microscopy
MIR	Mid infrared
MRI	Magnetic resonance imaging
NA	Numerical aperture

NADH	Nicotinamide adenine dinucleotide
NIR	Near infrared
NOPA	Noncollinear optical parametric amplifier
OCT	Optical coherence tomography
PBS	Phosphate buffered saline
PFA	Paraformaldehyde
ROI	Region of interest
SHG	Second harmonic generation
SNR	Signal to noise ratio
THG	Third harmonic generation
Ti:Sapph	Titanium-sapphire
WT	Wild type

INTRODUCTION

More complete data sets that robustly quantify the cellular microenvironment existing within the contracting myocardium are needed, requiring the development of new methods. As cardiac patient treatment strategies become more complicated and multifactorial, more sophisticated research techniques will help to bridge our gap in understanding, which has prohibited the next generation of treatment capable of restoring functional myocardium to an infarcted area from becoming commercialized. Current methods lack the ability to continuously record from subcellular transmural regions and deal with motion in a manner robust enough to study the coupling of multiple functional parameters, inhibiting the study of dynamic interaction of multiple cell types and study their response in pathology. Multiphoton microscopy, including two-photon and, more recently, three-photon microscopy enables imaging with cellular resolution. In addition, functional indicators such as calcium or voltage sensitive fluorescent indicators have been used with great success in brain to study the activity of single neurons within the intact, living animals. Such imaging could provide similar advantages of to the heart, but because the motion of the heart makes imaging challenging multiphoton microscopy has only recently been applied to intravital imaging of the heart.

There exist a growing number of intravital imaging techniques, which enable imaging at micrometer resolution in heart, but current methods have limitations that limit their utility, which quantification of physiology on disjointed spatial scales, however robust methods linking the behavior of individual cells to regional tissue performance in the same intravital imaging system are lacking. For example, Jung et al. used a suction-based GRIN imaging system which stabilized regions of tissue for imaging by applying a low pressure vacuum to the surface of the tissue (Jung, Kim et al. 2013). While this was well suited for repeat imaging and the pressure was found to

produce no damage histologically, the contractility of the tissue was hindered. The small field of view of the GRIN system also compromised the ability of the system to take measurements across large areas of tissue, reduced axial resolution, and was limited to imaging only at the tissue surface. Another group utilized more restrictive attachment methods such as imaging through the holes in a micro scale grid for the optical interface (Aguirre, Vinegoni et al. 2014). However, this also appeared to reduce tissue motion calling into question the relevance of the model to study the native contraction of the tissue. This grid also hindered the ability to simultaneously visualize large fields of view continuously.

Here, I developed a novel intravital imaging approach, which imposed minimal restriction on the motion of the tissue, provided high spatial resolution and maintained large fields of view, and used high speed imaging to overcome motion. A large clear aperture allowed for the use of a high NA objective for good spatial resolution. We found that motion, both axial and in-plane, was maintained, suggesting that the cardiomyocte contraction was not hindered by our approach. We demonstrated the first action potential recordings of individual cardiomyoctes within the ventricle wall in vivo, reported an endogenous contrast mechanism in atherosclerotic plaques, and explored the utility of three-photon excitation in the beating heart.

Chapter 2, on the discovery of third harmonic generation as a robust, endogenous contrast mechanism for detecting atherosclerotic plaques in extracted blood vessels, was published in Biomedical Optics Express.

> D. Small*, J. Jones*, I. Tendler, P. Miller, A. Ghetti, and N. Nishimura, "Label-free imaging of atherosclerotic plaques using third-harmonic generation microscopy", Biomed. Opt. Express 9, 214-229 (2018). *equal contributions

Chapter 3 was published in Frontiers in Physiology and has been reformatted for inclusion in this dissertation. This describes our new method for in vivo cardiac

imaging with two-photon microscopy. This enabled imaging and measurement of cardiac calcium indicators, cell motion and vascular dynamics in healthy and injured heart throughout the cardiac cycle.

> Jones J*, Small D*, Nishimura N, "In vivo calcium imaging and motion quantification in murine heart with multiphoton microscopy", bioRxiv 251561; doi: https://doi.org/10.1101/251561, in press, Frontiers in Physiology. *equal contributions

Chapter 4 explores optical properties of cardiac tissue in vivo that are required to choose optimum parameters for two- and three-photon microscopy. This chapter is the draft of the paper that will be submitted.

REFERENCES

Aguirre, A. D., et al. (2014). "Intravital imaging of cardiac function at the single-cell level." Proc Natl Acad Sci U S A **111**(31): 11257-11262.

Jung, K., et al. (2013). "Endoscopic time-lapse imaging of immune cells in infarcted mouse hearts." Circ Res **112**(6): 891-899.

CHAPTER 2

LABEL-FREE IMAGING OF ATHEROSCLEROTIC PLAQUES USING THIRD-HARMONIC GENERATION MICROSCOPY

2.1 Introduction

Atherosclerosis is characterized by the thickening and gradual accumulation of fat within the artery wall [1,2] and is a major cause of heart and cerebrovascular diseases worldwide [3,4]. Therefore, a greater understanding of the cellular mechanisms responsible for this condition, as well as less invasive and more sensitive technologies to monitor plaque formation in vivo is needed.

Current clinical techniques used to evaluate atherosclerosis include x-ray angiography [5-7], MRI [8-10], IVUS [11-13], and OCT [14-16]. Although these imaging strategies provide clinical information such as vessel morphology and, in some cases, thickness of the vessel wall, they are limited in their capacity to provide cell-scale resolution. For example, angiography, which shows the vessel lumen shape using an injected contrast agent, often fails to detect early wall composition changes that do not obstruct the lumen [17]. OCT and IVUS are able to detect changes within the vessel wall, but spatial resolutions are quite not sufficient to detect sub-cellular alterations during early plaque formation (axial resolutions of 150 – 200 μm and 10 – 18 μm for IVUS and OCT, respectively [13]). OCT and third harmonic generation (THG) signals both depend on index of refraction changes at interfaces. THG also depends on the χ^3 (3ω;ω,ω,ω) tensor, suggesting an additional mechanism based on chemical composition for contrast with THG [18]. Like OCT, imaging with THG microscopy in the clinic would require delivery of laser light and collection of signal through a catheter based system and would face similar engineering challenges. Open-heart surgery does provide a unique opportunity to optically image from the

surface of the ventricle down into the heart. In this case, it may be possible to use rigid endoscope type systems and avoid some of the engineering challenges associated with performing microscopy in a catheter.

The scientific understanding of atherosclerosis has primarily relied on histopathology and electron microscopy of post-mortem tissue [14,19-22]. Although high resolution and chemically specific, these techniques involve extensive tissue processing and cumbersome histological sectioning that may alter the structure and biochemical properties of the tissue. Multiphoton microscopy has emerged as an ideal imaging modality that is sensitive to specific molecules and structures in biological tissues [23-25] and can be used in vivo [26-31].

THG is an endogenous contrast mechanism, which facilitates in vivo experiments and opens up the possibility for clinical use. THG occurs when three photons at the excitation laser frequency are converted to one photon at three times the excitation frequency [32,33]. THG has been used in conjunction with two-photon excited fluorescence (2PEF) to image cellular lipid droplets [34], and myelin, a dense lipid sheath around axons, in the mouse brain and spinal cord [35]. It has been previously demonstrated that pure free fatty acid samples generate THG [36]. Seeger and colleagues have shown THG detection in a cross-sectional view of a histological section of atherosclerosis, but a better understanding of the signal source is needed [37]. We hypothesized that lipid structures in atherosclerotic plaques are an ideal application for THG imaging. Such imaging would be impactful in many applications due to the high prevalence and clinical significance of lipid bodies [1,38].

In this work, we demonstrate imaging of atherosclerotic lesions using label-free multiphoton microscopy with excitation in MIR range. Using a genetic knockout mouse model of atherosclerosis and diseased human coronary artery samples, we show the ability to produce detailed, three-dimensional and high-resolution optical

sections of atherosclerotic plaques. In addition to THG microscopy of lipid bodies, simultaneous SHG and autofluorescence show anatomical structures within label-free images. This technology is an important addition to the microscopy tool kit for studies of atherosclerosis.

2.2 Materials and methods

Test samples were harvested from mice lacking the apolipoprotein E gene ($ApoE^{-/-}$) which develop hypercholesterolemia and spontaneous atherosclerosis that closely mimics the human disease [39]. 2 – 4-month-old male and female $ApoE^{-/-}$ mice (n=4) (Jackson Labs Stock #002052) were fed a HFD for 16-weeks (Harlan TD.88137: protein 17.3%; carbohydrate 48.5%; fat 21.2% by weight). C57BL/6, age-matched, WT mice (n=3) fed a normal chow diet were used as controls. All animal care and experimental procedures were approved by the Institutional Animal Care and Use Committee of Cornell University and comply with the Guide for the Care and Use of Laboratory Animals by the National Institutes of Health.

To collect aortas, free-breathing mice were anesthetized with a mixture of 3% isoflurane gas in oxygen. A thoracotomy was performed, the right atrium punctured, and blood removed from the heart and aorta by perfusion of cold phosphate buffered saline (PBS) through the left ventricle until the perfusate was clear. This was followed by perfusion of cold 4% paraformaldehyde (PFA) in PBS. The heart and attached aorta (arch, thoracic and abdominal segments) were dissected and immersed in 4% PFA in PBS overnight, followed by 30% sucrose in PBS at 4°C. For whole mount imaging, the aortic arch was micro-dissected from the heart and thoracic aorta, then split lengthwise to expose the luminal surface. The aorta was placed on a glass slide, immersed in PBS with the luminal surface facing upwards and covered with a coverglass. For cryosections, aortas were frozen in Optimal Cutting Temperature

compound (Tissue-Tek, Sakura Finetek Inc.) and sectioned in a cryo-microtome with 7-μm or 20-μm thickness.

Human coronary arteries were provided by Anabios Corporation. All human tissues used for this study were obtained in the U.S.A. from organ donors following legal consent. Tissues were collected from one normal and one atherosclerotic heart. Tissues were derived from brain dead donors and the hearts removed at the same time as transplantable organs within an hour post cross-clamp. At the time of harvest, the human hearts were perfused with an ice-cold proprietary cardioplegic solution. Upon arriving in the laboratory, the heart was re-perfused with a proprietary recovery solution. Subsequently, sections of the coronary arteries were dissected using micro-scissors and tweezers, immediately fixed in 10% buffered formalin and then transferred to 70% ethanol after 24 hours and stored at 4º C. Approximately 12 months had passed from when the tissue had been placed in 70% ethanol. Prior to imaging, samples were immersed in 30% sucrose in PBS at 4º C for 1 week. Approximately 1-cm long sections of arteries were dissected from the provided sample, and macroscopic areas of plaque deposition were identified under a stereoscope. Sections of artery were further dissected around regions of plaque to obtain a flat sample. A coverglass was placed on the luminal surface and held in place with tape. PBS was added underneath the coverslip to prevent the sample from drying during imaging. After multiphoton imaging, samples were frozen and sectioned for histology.

Serial cross-sections of human and mouse aortas were stained with hematoxylin and eosin (H&E) and Masson's Trichrome for collagen using standard procedures [40]. For Nile-Red staining of lipids, 20-μm sections of aortas from ApoE-/--HFD were immersed in 5 μg/mL Nile-Red diluted in PBS for 30 min at room temperature. Sections were washed thoroughly in PBS and then coverslipped in PBS.

CD68 immunofluorescence was performed on 7-μm human coronary artery sections to identify regional macrophage and foam cell location and its relationship to THG signal. Sections were incubated in 1% sodium dodecyl sulfate in PBS for 5 min. To block non-specific binding, blocking buffer (3% bovine serum albumin, 10% goat serum, 0.1% Triton X-100 in PBS) was added for 30 min. Sections were then incubated with CD68 primary antibody (1:50, sc-20060; Santa Cruz Biotechnology Inc.) diluted in blocking buffer overnight at 4°C. Following three washes in PBS, goat anti-mouse Alexa-Fluor 594 secondary antibody (1:200, A11005; Thermo Scientific) was applied diluted in PBS for 30 min at room temperature. Slides were then washed, and mounted with aqueous mounting medium containing DAPI for cell nuclei (Vectashield, H-1200; Vector Laboratories). Confocal microscopy was performed on a Zeiss LSM880 Confocal inverted microscope using a Zeiss plan apochromatic 40x 1.4 NA oil objective controlled by ZEN 2.1 SPC software. Laser lines for DAPI and Alexa-594 were 405 nm and 561 nm respectively, and signal was collected between 410–496 nm (DAPI) and 588–733 nm (Alexa-594).

Imaging was conducted using a custom multiphoton microscope equipped with four epi-detection backward scattered channels, the option of two MIR sources used for harmonic generation, as well as a Ti:Sapph oscillator (Chameleon, Coherent) for 2PEF. 1,700-nm laser light (~100-fs pulse length, 40-nm full-width-half-max (FWHM) bandwidth) was produced through a soliton self-frequency shift of 1,550-nm femtosecond pulses from a commercial fiber laser (FLCPA-02CCNU15, Calmar Lasers) through a photonic crystal rod with a fundamental mode area of 3500 μm2 (NC420-152-EE45, NKT Photonics). For 1,700-nm lasers, dispersion is compensated using stacked silicon wafers (University Wafer ID# 2808) set at Brewster's angle [41]. To generate 1,300 nm laser light, a noncollinear optical parametric amplifier (NOPA) (Coherent, Opera-F) was seeded by a diode-pumped femtosecond laser (60 μJ/pulse at

1 MHz; Coherent, Monaco). Dispersion for 1,300-nm excitation was compensated with an SF11 prism pair [27]. For imaging, the excitation laser was scanned with a line rate of ~1kHz with galvanometric scanners. Images were acquired with an Olympus XLPlan N 25x 1.05 NA objective customized for MIR excitation wavelengths. Images of 0.175 ± 0.005 μm diameter microspheres (PS-Speck Microscope Point Source Kit P7220) had intensities profiles with the full-width half max of 3.39 μm axial and 0.85 -μm lateral with 1,300 nm and WWW 2.64 μm lateral and 2.02 μm axial with 1,700 nm. When imaging with 1,700 nm, heavy water (D2O) was used for index matching between the coverglass and the objective in order to minimize absorption of the excitation light [41]. For 2PE microscopy of Nile-Red, images were acquired using a Ti:Sapph laser with the wavelength centered at 810 nm using an off-the-shelf Olympus XLPlan N 25x 1.05 NA objective. Signal was collected using custom detections optics using a primary dichroic suited for either MIR or NIR (near-infrared) laser transmission (BLP01-980R-49x70, FF705-Di01-49x70, Semrock), secondary dichroic (FF01-593/LP-90x108, Semrock), two tertiary dichroic (FF801-Di02-90x108, Di02-R488-90x108, Semrock), and bandpass filters on each detection channel (FF01-433/24-25, Semrock, FF01-560/25-25, Semrock, NC528423 – ET645/65m, Chroma, and FF01-834/LP-25, Semrock). For each ApoE-/- mouse or human coronary artery sample, 3 – 6 z-stacks were taken within different regions of the same sample. 512 x 512 pixel frames were acquired at 1.8 frames/sec (dwell time of 2 μs/pixel). Therefore a 400-μm scan volume took approximately two minutes to complete. All images were processed using ImageJ (National Institutes of Health). Projections were maximum intensity projections over thicknesses noted in the caption. Images for display were background subtracted (rolling ball radius, 50 pixels) and a median filter (2 pixels) was applied. Contrast was adjusted for each image manually by adjusting the

maximum and minimum displayed values while maintaining a linear intensity relationship within the displayed range.

2.3 THG of atherosclerotic plaques

We imaged whole-mounted aortas, illuminated from either the luminal or abluminal side of the tissue, from a mouse model of atherosclerosis fed a high-fat diet for 16 weeks in regions where plaques were visible by eye and similar regions from wild type mice fed normal diets as control. All ApoE-/- (4 mice) samples contained atherosclerotic plaques and no WT samples (3 mice) contained atherosclerosis. Only atherosclerotic regions in ApoE-/- mice were imaged. Using multiphoton microscopy excited with 1,700 nm excitation (1 MHz, less than 35 mW at surface) several nonlinear optical processes provide contrast that distinguish morphological features throughout the healthy and diseased vessel wall. In both atherosclerotic and control samples, SHG, detected at 802 – 835 nm, was present at the outer adventitial surface and was spatially and morphologically consistent with collagen fibers (Fig. 1a and c). A striated pattern with the broad spectral emission of elastin autofluorescence was visible within the vessel walls at 613–678 nm and within the THG range (548–573 nm) (Fig. 1c-ii.). Aortas from ApoE-/--HFD mice had distinct, bright, globular structures in the THG spectral emission range of 548 – 573 nm near the luminal surface (Fig. 1a-i) and deeper with the vessel wall at levels with the elastin autofluorescence (Fig. 1a-ii). Comparison to histological sections of the same treatment group (Masson's Trichrome and H&E staining, Fig. 1b) revealed lipid deposits within the tunica intima that appear similar in morphology to deposits in multiphoton microscopy cross-sectional views. Such structures were not present in WT-Normal aortas (Fig. 1c and d).

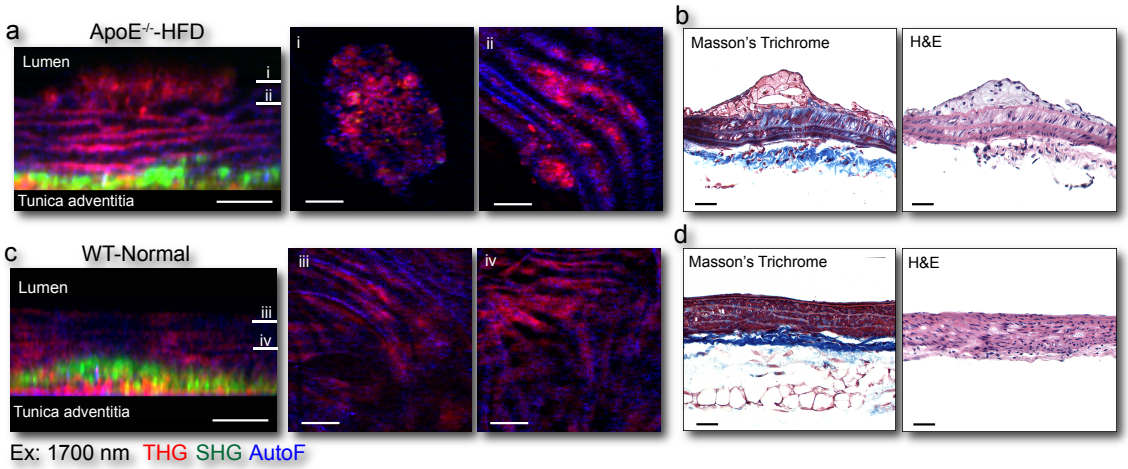

Figure. 1. Multiphoton microscopy shows vessel wall structures consistent with atherosclerotic lesions in whole-mounted aortas extracted from a murine model of atherosclerosis. (a) Aorta from an apolipoprotein E knockout mouse fed a high fat diet (ApoE-/--HFD) shown with cross-sectional and enface views (i and ii) through a region with strong emission at the third harmonic generation (THG) wavelengths. Laser excitation was at 1,700 nm, incident on the lumen. (b) Histology with Masson's trichrome and H&E staining of aorta from an ApoE-/--HFD mouse. (c) Aorta from a wild type mice fed a normal chow diet (WT-Normal) and cross-sectional and enface views (iii and iv). (d) Histology of aorta from a WT-Normal mouse. Cross-sectional views in a and c are maximum intensity projections through the y-axis. Second harmonic generation (SHG); autofluorescence (AutoF). Scale bars are 50 µm.

To confirm that the source of THG is from lipids, Nile-Red was used to stain lipids in ApoE-/--HFD tissue sections (3 ROI from 2 mice). Imaging of the same region of interest using 2PEF for Nile-Red (Fig. 2a: Ex: 810 nm; Em: 612–677 nm) and 1,700 nm excitation light for THG (Em: 535–585 nm), demonstrated that the structures with strong THG signal also have strong Nile-Red signal (Fig. 2b), suggesting that the source of THG is the lipids within atherosclerotic plaques.

Multiphoton microscopy using 1,300 nm excitation showed similar structures as 1,700 nm excitation in the vessel wall and at the luminal surface in the THG spectral range of 421–445 nm (Fig. 3a and b). Unlike fluorescence, the wavelength of THG depends on the excitation wavelength. Therefore, to identify the features giving rise to THG, 1,300-nm and 1,700-nm excitation were used to image the same ApoE-/--

HFD sample at a region that had atherosclerotic features. Emission channels that included the THG wavelengths, 421–445 nm for 1,300 nm and 548–573 nm for 1,700 nm, generated similar images, while the alternate channels showed little signal (Fig. 3a). This change in emission wavelengths is consistent with THG.

WT-Normal aortas generally appeared similar, even between different mice (Fig. 4a and Fig.1c). Consistent structures included the medial layer that primarily consists of smooth muscle cells and elastin that generated autofluorescence and a weak THG signal (Fig. 4a-ii). Collagen of the tunica adventitia produced SHG in both normal and

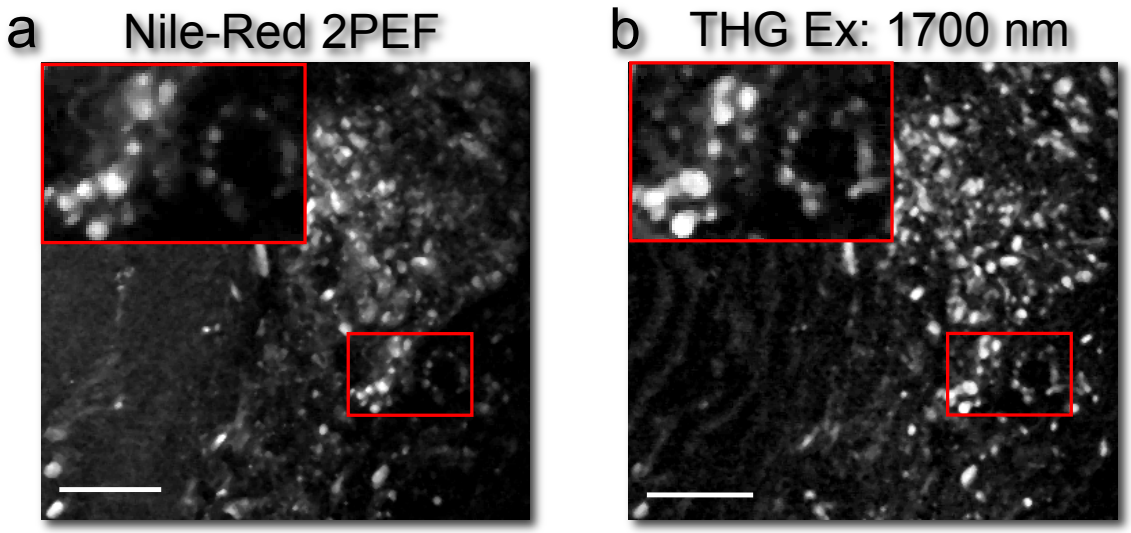

Figure 2. Correlation between third harmonic generation (THG) and lipid stain. (a) Frozen section (20-µm thickness) of aorta from ApoE-/--HFD stained for lipids using Nile-Red and imaged using two-photon excited (2PE) at 810 nm excitation. Displayed image shows fluorescence channel for Nile-Red (612–677 nm). (b) Same section imaged with 1,700 nm excitation showing the THG channel detected with 548–573 nm band pass filter. Scale bars are 50 µm.

atherosclerotic samples (Fig. 4a-iii and b-iii). THG on the abluminal side of the vessel was due to adventitial fat that was sometime present following aorta dissection (Fig. 4b) and was closely associated with SHG in the adventitial layer.

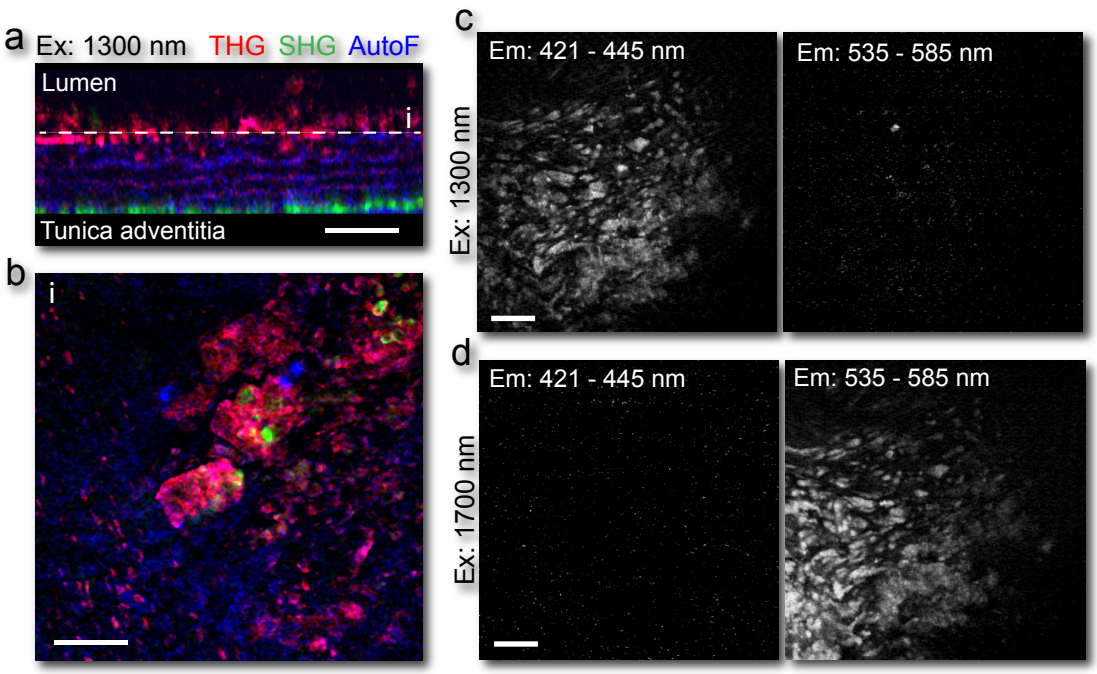

Figure 3. Optical properties of atherosclerotic lesions in mouse aorta. (a and b) 1,300 nm excitation produces signals at third harmonic generation (THG) and second harmonic generation (SHG) wavelengths as well as autofluorescence (AutoF) at an atherosclerotic lesion. Cross-sectional, maximum projected (a) and enface (b) views of ApoE-/--HFD aorta. Line in a shows location of b. (c) 1,300 nm excitation of a region within ApoE-/--HFD aorta that has atherosclerotic features, produces a strong signal in the THG emission range (421–445 nm). (d) 1,700 nm excitation of the same region shows the same features in the THG emission range (548–573 nm). Scale bars are 50 μm.

ApoE-/--HFD arteries displayed highly variable morphologies and features even within the same mouse. In an example of pathology that extended across a wide area, THG appeared in scattered, smaller patches throughout the luminal half of the vessel wall (Fig. 4b). THG clearly identified an area of intimal thickening of ApoE-/--HFD vessel wall by the presence of punctate regions indicating lipids (Fig 4b-i) that are not present in WT-Normal (Fig. 4a-i). Different samples revealed a variety of

plaque features that could be detected with THG imaging (Fig. 4c-f). Furthermore, different size and structures of plaque development can be observed between the same sample within different regions. THG signals varied from continuous large deposits near the lumen (Fig. 4c) to punctate regions of lipid deposits about 8 µm in size within deeper layers of the intima (Fig. 4d and e). Images from a region of vessel bifurcation

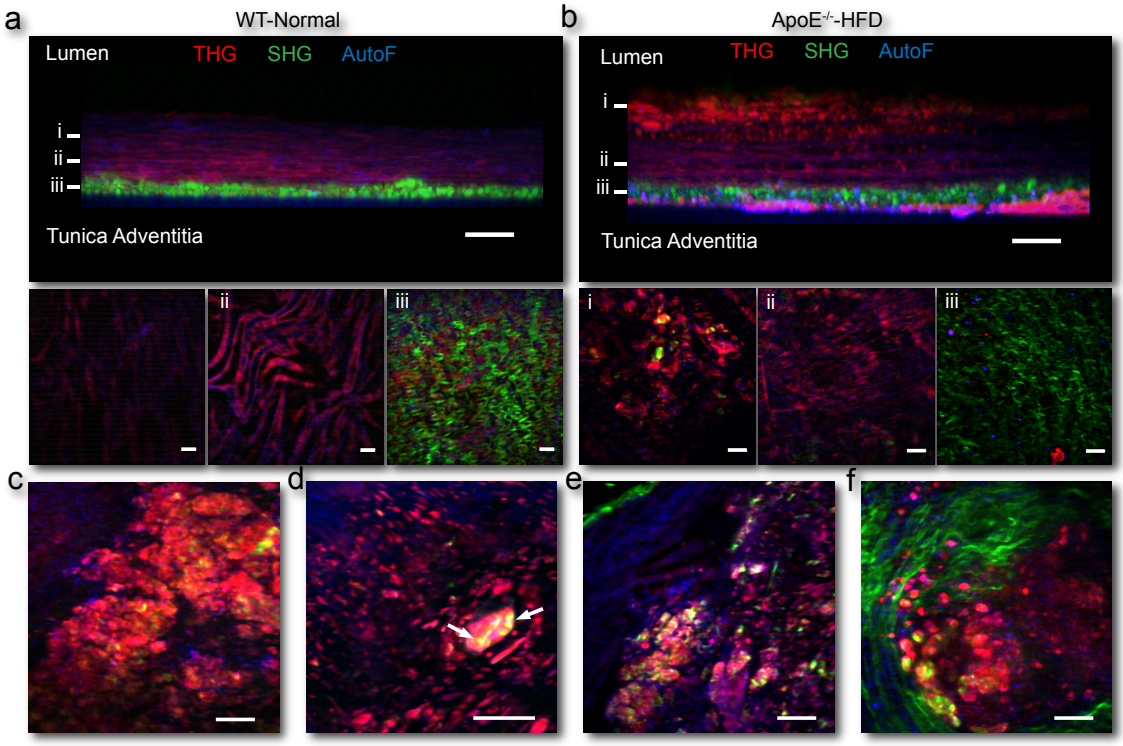

Figure 4. Third harmonic generation (THG) microscopy using 1,700 nm excitation reveals varying features of atherosclerotic lesions. (a) WT-Normal and (b) ApoE-/--HFD mouse aortas shown in cross-sectional projections and enface views, show second harmonic generation (SHG) of the tunica adventitia (a-iii and b-iii), autofluorescence (AutoF) in the media (a-ii and b-ii) and a strong THG signal within the thickened intimal layer of ApoE-/--HFD (b-i) that is not present in WT-Normal (a-i). Single z-slices through different lesions (c-f) show variability in structures producing THG signal and the association between SHG, THG and AutoF. (c) Large deposit of THG signal 38 µm below lumen. (d) Small punctate regions of THG signal 48 µm below lumen, with SHG positioned in close association with THG (arrows). (e) Image from near the abluminal edge of aorta showing THG and SHG deposits. (f) Plaque near a vessel bifurcation off of the aortic arch. Scale bars are 50 µm.

from the aortic arch (Fig. 4f), revealed similar structures and signals within the tissue - THG at the luminal surface, then elastin and collagens revealed by autofluorescence and SHG towards the abluminal surface, respectively. Occasionally, SHG was detected in close association within larger THG regions of plaques (Fig. 4, arrows). Fig. 4f also shows the detection of SHG (collagen) within the medial layer in close association with autofluorescence. Both 1,300 nm and 1,700 nm excitation sources were able to image through the entire vessel wall of ApoE-/- and WT mice (70 – 150 μm).

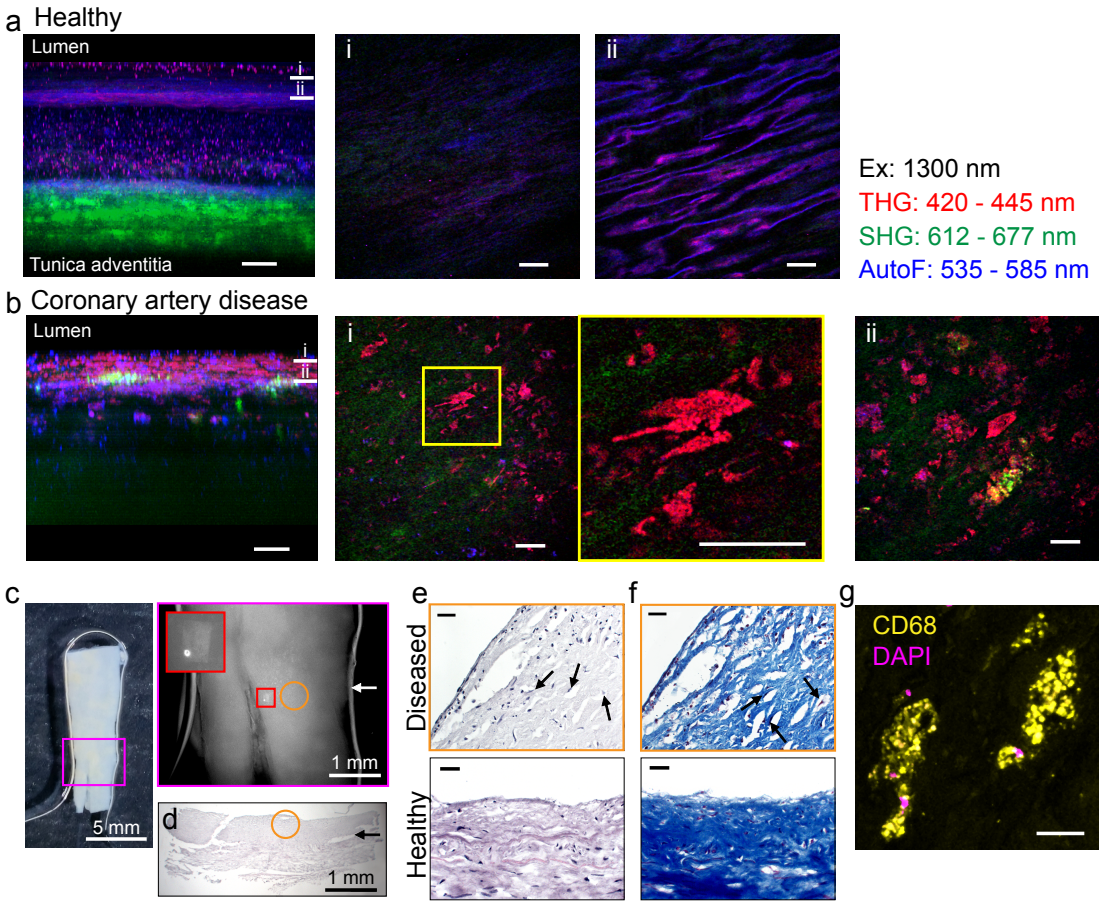

Figure 5. Third harmonic generation (THG) microscopy of human coronary artery. (a) In a healthy coronary artery imaged from the luminal side with 1,300 nm excitation, a cross-sectional projection and enface planes (i and ii) show second harmonic generation (SHG) and broad autofluorescence (AutoF) throughout the intimal layer. (b) An artery sample with coronary artery disease imaged from the luminal side with 1,300 nm. i and ii show images from levels indicated in cross-

sectional view. Yellow box shows location of magnified view. (c) Photograph and epi-fluorescence image of sample imaged in (b). Magenta box shows the locations of magnified regions. A small laser burn (red box) was induced during THG microscopy at a measured displacement to the imaged region in (b) indicated with an orange circle to aid in image registration. A 23-gauge needle was used to make a fiduciary mark (arrows). (d) Bright-field image of region imaged with multiphoton microscopy from a section of the tissue with fiduciary mark (black arrow). (e) Higher magnification images from the region imaged with multiphoton microscopy stained with H&E and (f) Masson's Trichrome. Open, nucleated spaces (arrows) are consistent with lipid deposits. Sections from a sample with no atherosclerosis (healthy) are shown below. (g) Confocal microscopy of immunostaining for CD68 in a section from the same region. Unless otherwise noted, scale bars are 50 μm.

2.4 Human coronary artery THG imaging

We used THG microscopy (1,300 nm) to demonstrate the capability to image atherosclerosis within a human coronary artery (Fig. 5). Two different human coronary artery samples were imaged with THG microscopy, a healthy coronary artery (Fig. 5a) and a coronary artery that had been classified as coronary artery disease and had macroscopically visible plaques (Fig. 5b). When mounted with the lumen side towards the objective, we were able to image through the entire 270-μm thickness of the healthy coronary artery wall from the intima to the adventitia. Intrinsic contrast mechanisms showed characteristic features of the vessel wall similar to mouse aorta. This included SHG of collagen fibers within the adventitia, and autofluorescence from elastin that was particularly evident within the internal elastin lamina (Fig 5a-ii).

In the coronary artery disease sample, the imaging depth when imaged from the lumen was limited to the intima and media layers and reached 400 μm in depth. Like in the mouse aorta, THG appeared in distinct patches within intimal layers. Some THG patches showed granular structures (~3-μm nodules) with THG signal suggesting a sub-cellular source (Fig 4b-i and b-ii). Throughout intimal and medial layers, weak, diffuse SHG and autofluorescent signal were present in regions around THG-emitting deposits. In some locations in the intima, SHG appeared in clusters of bright, 30 – 70 μm spots (Fig. 5b-ii). To confirm the presences of atherosclerotic

lesions in this tissue, we sectioned and stained the sample. For registration of the multiphoton microscopy images to histological sections, a small laser burn was induced at a measured displacement from the imaged region during THG imaging (Fig. 5c). Wide-field fluorescence microscopy of the intrinsic autofluorescence was used to find the marked region. With this image for positioning, a 23-gauge needle was inserted into the side of the tissue as a fiducial to identify sections taken through the imaged region for histological processing (Fig. 5d). H&E staining revealed clear spaces within the imaged region, characteristic of macrophage foam cells that previously in vivo contained lipids and are marked by a remaining nucleus (Fig. 5e) [42]. Masson's Trichrome staining revealed similar structures and collagen throughout the lesion (Fig. 5f). Healthy control tissue did not show these features. Immunofluorescence confirmed the presence of CD68-positive macrophage foam cells within the imaged region that showed similarly-shaped, THG-positive structures (Fig. 5g). H&E, Masson's Trichrome and CD68 immunofluorescence was performed on two additional histological sections and the same result was observed (data not shown).

2.5 Discussion

Despite significant advances in the understanding and clinical monitoring of vessel wall pathology in coronary artery disease, atherosclerosis remains a major health problem. We have demonstrated that a strong THG signal is generated from atherosclerotic plaques in both rodent and human artery samples. Used in conjunction with other nonlinear optical processes such as SHG and autofluorescence, this technique could be used to characterize atherosclerotic lesions in label-free tissue.

We observed a range of structures with THG signal in diseased vessels that resemble features found in standard histological classification of atherosclerotic plaques [2,43,44] (Fig. 6). The THG-producing structures that we observed are similar in

morphology to lipid-containing features found in the earlier stages. Intimal macrophages play a key role in the pathogenesis of atherosclerosis, especially during the initial stages of development [45]. Sub-cellular, punctate THG signal was observed within the intima of mouse (Fig. 1 and 3) and human coronary artery (Fig. 5b), near the junction of the media, and appeared similar to small lipid deposits reported within early macrophage foam cells in intimal xanthomas and pathologic intimal thickening [44]. Histological staining in both mouse and human samples confirmed the presence of macrophages in regions with THG structures. The gradual accumulation of lipids within macrophages in accompanied by increased expression of surface scavenger receptors such as CD68 [45]. In both mouse and human, THG puncta also clustered in groups forming patches of 50 – 100 μm. We found CD68-positive macrophages near THG deposits that had similar morphology to these patches. Continual uptake of lipids increases the size of macrophage foam cells leading to the degradation of macrophage cell components and development of extracellular lipids pools [46]. Intermediate lesions and fibrous cap atheromas are identified by extracellular lipid pools within the intima [44], which have a similar morphology to that detected by THG microscopy in some samples (Fig. 3c). SHG detected in some regions of plaques (Fig. 4d and 5b) could be due to accumulated cholesterol crystals. Work by Suhalim and colleagues [47], demonstrated that SHG can arise from chiral cholesterol molecules in the crystal lattice of cholesterol crystals within atherosclerotic plaques. Alternatively, SHG is strongly generated by collagen and advanced lesions consist of fibrous connective tissue primarily composed of collagens overlying a lipid pool [43]. However, SHG detected in these regions did not take the shape of a collagen-rich cap on top of lipid, thus may represent the early stages of collagen deposition.

SHG [48] and 2PEF microscopy [49,50] have previously been used to study atherosclerosis, but imaging with a laser source that enabled efficient higher order

nonlinear processes added novel contrast mechanisms. We demonstrated that autofluorescent signals in both rodent and human atherosclerotic samples using MIR excitation showed structures similar to those seen with 2PEF using NIR and therefore can be used to provide anatomical cues and reference points [24,49-51]. Similar to 2PEF, the likely source of autofluorescence within the medial layer of vascular tissue is elastin. Elastin is arranged circumferentially around the vessel lumen in an undulatory pattern [49], has broad emission [24], and matches histology of mouse and human tissue. NADH within smooth muscle cells interspersed with elastin may also contribute to the autofluorescent signal [51]. This source of autofluorescence adds further contrast, aiding the interpretation of atherosclerotic pathology of the vessel wall. For experimental studies of atherosclerosis, exogenous dyes and transgenic rodent models have been used to label structural components and cell types with 2PEF [49,52-54], and may also be used with THG-compatible sources with both two- and three-photon excitation. Previously, two-photon excited autofluorescence of oxidized low-density lipoproteins has been demonstrated and is likely a contributing signal within the atherosclerotic plaque [55]. THG is strongly enhanced at discontinuities in refractive index, so that the strength of the signal in atherosclerotic plaques may in part come from interfaces and structures with the plaques. Some caution is required in interpretation of the THG signal, because it is not specific only to lipids and the signal from atherosclerotic plaques is likely a combination of THG and fluorescence from various sources [24,55]. Seeger and colleagues used THG to discern tissue morphology in a histological cross-section of human carotid artery atheroma using 1,043 nm excitation [37]. However, this system utilized forward scattering THG signal collection, presumably due to stronger attenuation of the shorter 1,040-nm excitation and the resulting third harmonic, and required a thin 10-μm histological cross-section, rather than the whole tissue preparation used in the current study. The use of higher

wavelength excitation at 1,300 nm and 1,700 nm significantly improves the THG signal due to decreased attenuation at these wavelengths. This enables imaging through the vessel wall in both murine and human models, which is important for the in vivo use and translatable potential of this technology.

Although there are differences between mouse models and human, we were able to see similar structures in both species [39] which suggests that this imaging modality could be used for label-free imaging in clinical applications. THG microscopy using high peak-power, low repetition-rate lasers may offer an alternate and advantageous approach in the clinical observation of atherosclerosis. Intravascular OCT has had significant adoption for the clinical detection and study of atherosclerosis and can image at sufficient depths (1 – 3 mm) [14-16], however is limited in its diagnostic capabilities to define key plaque features such as lipids, that present as low OCT signal. The capability of OCT to differentiate non-necrotic intracellular and extracellular lipid accumulations from necrotic core lipid remains a challenge [56]. The ability to detect these lipid features would aid the classification of vulnerable lesions. A number of studies have combined OCT with 2PE of endogenous species, which has improved the structural and molecular analysis of atherosclerotic plaques, often detecting autofluorescence of oxidized lipids within plaques of vulnerable regions [57,58]. While THG-imaging using MIR excitation provides similar information, it does so with enhanced imaging depth that may be needed to assess thicker atheromas which may circumvent the need to combine with another imaging modality. Coherent anti-Stokes Raman (CARS) microscopy has also been shown to be effective at detecting lipid-rich structures [59] including lipids within atherosclerotic plaques and has better chemical specificity than THG since it is based on specific chemical bonds [52,60]. Unfortunately, CARS requires spatial and temporal overlap of two ps lasers at different wavelengths [61,62] which remains a

technical challenge that limits the widespread uptake of CARS as an in vivo imaging modality. Furthermore, intimal xanthomas represent early vessel pathology [44] that can only be detected microscopically. Study of these lesions are often restricted to post-mortem sampling, therefore a significant void exists in understanding the initiating cell interactions during these early stages in vivo.

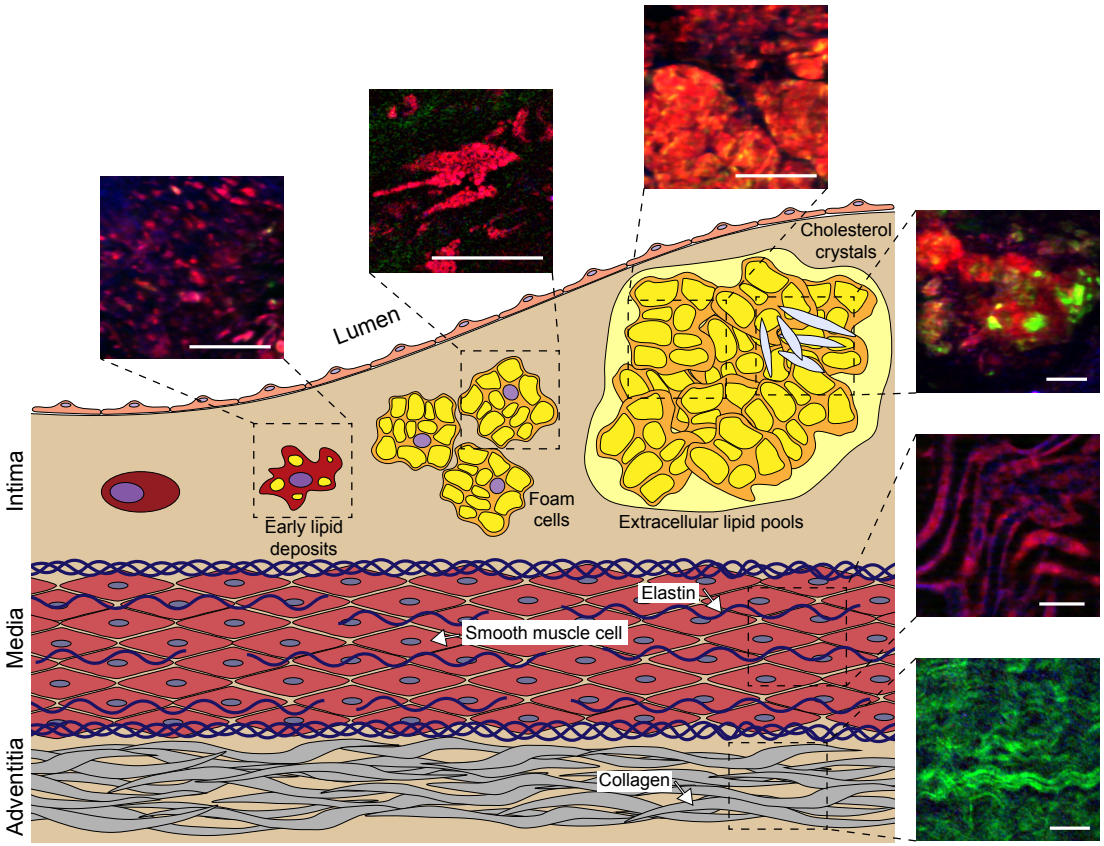

Figure 6: Summary of morphological features revealed by third harmonic generation (THG) microscopy. Small lipid deposits accumulate in monocytes of the intima during the initial stages of atherosclerosis and can be detected with THG as punctate regions within the intima. Continual uptake of atherogenic lipids increases the size of cellular lipid deposits leading to the formation of foam cells, that are characterized by a cytoplasm filled with lipids. Extracellular lipid pools develop following the breakdown of cellular components and appear with THG imaging as larger regions. Second harmonic generation (SHG) within extracellular lipid pools are most likely cholesterol crystals. Additional nonlinear optical processes simultaneously provide contrast of components of the medial layer (elastin and smooth muscle) and collagens within the adventitia. Red is THG, green is SHG, and blue is autofluorescence. Scale bars are 50 μm.

Multiphoton microscopy with THG is just one among several technologies which have the potential to study atherosclerosis in vivo. Time-resolved laser-induced fluorescence spectroscopy has been successfully used to detect the biochemical properties of atherosclerotic plaques in patients [63-65]; novel contrast agents such as plasmonic gold nanorods have been used to monitor macrophage distribution in vulnerable plaques [66-68]; and a wide variety of strategies combining different imaging modalities such as OCT, 2PEF, optoacoustic microscopy, and CARS have been used successfully [57,58,69-71]. However, associated toxicities of contrast agents, as well as technical complexity of combining multiple imaging systems, has slowed the practical uptake of new imaging modalities for in vivo detection of atherosclerosis. An imaging modality that utilizes endogenous contrast mechanisms from a single excitation source presents an attractive option for in vivo atherosclerosis imaging.

Although THG imaging has been demonstrated previously, new MIR fs laser sources now make THG imaging feasible for widespread adoption. Advantages of new lasers include a higher peak power, which is critical for higher-order nonlinear excitation, and longer wavelengths, both of which enable greater depth of imaging [72,73]. Laser sources based on photonic crystal fibers around 1,700 nm have been developed specifically for these applications [74]. Additionally, new and commercially available excitation sources provide turn-key optical parametric amplifiers which allow labs with limited technical knowledge to tune from 1 – 2 μm, that has been unachievable until recently.

THG imaging will likely be readily used in experimental multiphoton microscopy. However, clinical translation will require new advancements to overcome limitations of the current study. This includes the fact that imaging was performed on ex vivo post-fixed tissue under a microscope, and our acquisition scheme was not

optimized for intravascular imaging. Improvement in the depth of imaging may also be achievable with currently available methods [72,75,76]. The potential of THG microscopy as a clinical tool depends on the continued progress in development of MIR laser scanning probes [57,58,77-80].

2.6 Conclusion

New imaging technologies are required that provide high resolution three-dimensional information at sufficient depth to understand and diagnose the heterogeneity of atherosclerosis. Using high peak power, low-repetition laser sources in the MIR range of excitation, it is possible to generate THG from cellular and extracellular lipids in atherosclerotic plaques. Similar studies of atherosclerosis have combined nonlinear optical process (e.g. SHG and endogenous fluorescence) with another imaging modality, such as CARS, to image lipid content. Advantages of the current technique are that the nonlinear optical processes are generated from a single laser source, thereby decreasing the complexity and increasing practicality. THG could be useful for studies that aim to understand the cellular basis for atherosclerosis and lipid deposition. Given the increased practicality of THG imaging and our demonstration of its use in human coronary artery disease, this technique holds potential to be investigated as a clinical tool.

REFERENCES

[1] H. C. Stary, A. B. Chandler, R. E. Dinsmore, V. Fuster, S. Glagov, W. Insull, Jr., M. E. Rosenfeld, C. J. Schwartz, W. D. Wagner, and R. W. Wissler, "A definition of advanced types of atherosclerotic lesions and a histological classification of atherosclerosis. A report from the Committee on Vascular Lesions of the Council on Arteriosclerosis, American Heart Association," Circulation 92, 1355-1374 (1995).

[2] H. C. Stary, A. B. Chandler, S. Glagov, J. R. Guyton, W. Insull, Jr., M. E. Rosenfeld, S. A. Schaffer, C. J. Schwartz, W. D. Wagner, and R. W. Wissler, "A definition of initial, fatty streak, and intermediate lesions of atherosclerosis. A report from the Committee on Vascular Lesions of the Council on Arteriosclerosis, American Heart Association," Circulation 89, 2462-2478 (1994).

[3] D. Mozaffarian, E. J. Benjamin, A. S. Go, D. K. Arnett, M. J. Blaha, M. Cushman, S. de Ferranti, J. P. Despres, H. J. Fullerton, V. J. Howard, M. D. Huffman, S. E. Judd, B. M. Kissela, D. T. Lackland, J. H. Lichtman, L. D. Lisabeth, S. Liu, R. H. Mackey, D. B. Matchar, D. K. McGuire, E. R. Mohler, 3rd, C. S. Moy, P. Muntner, M. E. Mussolino, K. Nasir, R. W. Neumar, G. Nichol, L. Palaniappan, D. K. Pandey, M. J. Reeves, C. J. Rodriguez, P. D. Sorlie, J. Stein, A. Towfighi, T. N. Turan, S. S. Virani, J. Z. Willey, D. Woo, R. W. Yeh, M. B. Turner, C. American Heart Association Statistics, and S. Stroke Statistics, "Heart disease and stroke statistics--2015 update: a report from the American Heart Association," Circulation 131, e29-322 (2015).

[4] G. K. Hansson, "Inflammation, atherosclerosis, and coronary artery disease," N Engl J Med 352, 1685-1695 (2005).

[5] M. A. Latif and M. J. Budoff, "Role of CT angiography for detection of coronary atherosclerosis," Expert Rev Cardiovasc Ther 12, 373-382 (2014).

[6] A. Thomassen, H. Petersen, A. C. Diederichsen, H. Mickley, L. O. Jensen, A. Johansen, O. Gerke, P. E. Braad, P. Thayssen, M. M. Hoilund-Carlsen, W. Vach, J. Knuuti, and P. F. Hoilund-Carlsen, "Hybrid CT angiography and quantitative 15O-water PET for assessment of coronary artery disease: comparison with quantitative coronary angiography," Eur J Nucl Med Mol Imaging 40, 1894-1904 (2013).

[7] D. D. Adraktas, E. Tong, A. D. Furtado, S. C. Cheng, and M. Wintermark, "Evolution of CT imaging features of carotid atherosclerotic plaques in a 1-year prospective cohort study," J Neuroimaging 24, 1-6 (2014).

[8] R. Corti and V. Fuster, "Imaging of atherosclerosis: magnetic resonance imaging," Eur Heart J 32, 1709-1719b (2011).

[9] C. Yuan, L. M. Mitsumori, M. S. Ferguson, N. L. Polissar, D. Echelard, G. Ortiz, R. Small, J. W. Davies, W. S. Kerwin, and T. S. Hatsukami, "In vivo accuracy of multispectral magnetic resonance imaging for identifying lipid-rich necrotic cores and intraplaque hemorrhage in advanced human carotid plaques," Circulation 104, 2051-2056 (2001).

[10] Z. A. Fayad, T. Nahar, J. T. Fallon, M. Goldman, J. G. Aguinaldo, J. J. Badimon, M. Shinnar, J. H. Chesebro, and V. Fuster, "In vivo magnetic resonance evaluation of atherosclerotic plaques in the human thoracic aorta: a comparison with transesophageal echocardiography," Circulation 101, 2503-2509 (2000).

[11] K. W. Moon, J. H. Kim, K. D. Yoo, S. S. Oh, D. B. Kim, and C. M. Kim, "Evaluation of radial artery atherosclerosis by intravascular ultrasound," Angiology 64, 73-79 (2013).

[12] D. Bose, C. von Birgelen, and R. Erbel, "Intravascular ultrasound for the evaluation of therapies targeting coronary atherosclerosis," J Am Coll Cardiol 49, 925-932 (2007).

[13] J. Ge, F. Chirillo, J. Schwedtmann, G. Gorge, M. Haude, D. Baumgart, V. Shah, C. von Birgelen, S. Sack, H. Boudoulas, and R. Erbel, "Screening of ruptured plaques in patients with coronary artery disease by intravascular ultrasound," Heart 81, 621-627 (1999).

[14] H. G. Bezerra, M. A. Costa, G. Guagliumi, A. M. Rollins, and D. I. Simon, "Intracoronary optical coherence tomography: a comprehensive review clinical and research applications," JACC Cardiovasc Interv 2, 1035-1046 (2009).

[15] H. Yabushita, B. E. Bouma, S. L. Houser, H. T. Aretz, I. K. Jang, K. H. Schlendorf, C. R. Kauffman, M. Shishkov, D. H. Kang, E. F. Halpern, and G. J. Tearney, "Characterization of human atherosclerosis by optical coherence tomography," Circulation 106, 1640-1645 (2002).

[16] A. Tanaka, T. Imanishi, H. Kitabata, T. Kubo, S. Takarada, H. Kataiwa, A. Kuroi, H. Tsujioka, T. Tanimoto, N. Nakamura, M. Mizukoshi, K. Hirata, and T. Akasaka, "Distribution and frequency of thin-capped fibroatheromas and ruptured plaques in the entire culprit coronary artery in patients with acute coronary syndrome as determined by optical coherence tomography," Am J Cardiol 102, 975-979 (2008).

[17] R. B. Singh, S. A. Mengi, Y. J. Xu, A. S. Arneja, and N. S. Dhalla, "Pathogenesis of atherosclerosis: A multifactorial process," Exp Clin Cardiol 7, 40-53 (2002).

[18] R. M. Boyd, Nonlinear Optics, 3 ed. (2008).

[19] R. F. Barth, D. A. Kellough, P. Allenby, L. E. Blower, S. H. Hammond, G. M. Allenby, and L. M. Buja, "Assessment of atherosclerotic luminal narrowing of

coronary arteries based on morphometrically generated visual guides," Cardiovasc Pathol 29, 53-60 (2017).

[20] J. Wang, C. Sun, N. Gerdes, C. Liu, M. Liao, J. Liu, M. A. Shi, A. He, Y. Zhou, G. K. Sukhova, H. Chen, X. W. Cheng, M. Kuzuya, T. Murohara, J. Zhang, X. Cheng, M. Jiang, G. E. Shull, S. Rogers, C. L. Yang, Q. Ke, S. Jelen, R. Bindels, D. H. Ellison, P. Jarolim, P. Libby, and G. P. Shi, "Interleukin 18 function in atherosclerosis is mediated by the interleukin 18 receptor and the Na-Cl co-transporter," Nat Med 21, 820-826 (2015).

[21] I. Perrotta, "Ultrastructural features of human atherosclerosis," Ultrastruct Pathol 37, 43-51 (2013).

[22] I. A. Sobenin, M. A. Sazonova, A. Y. Postnov, Y. V. Bobryshev, and A. N. Orekhov, "Changes of mitochondria in atherosclerosis: possible determinant in the pathogenesis of the disease," Atherosclerosis 227, 283-288 (2013).

[23] W. R. Zipfel, R. M. Williams, and W. W. Webb, "Nonlinear magic: multiphoton microscopy in the biosciences," Nat Biotechnol 21, 1369-1377 (2003).

[24] W. R. Zipfel, R. M. Williams, R. Christie, A. Y. Nikitin, B. T. Hyman, and W. W. Webb, "Live tissue intrinsic emission microscopy using multiphoton-excited native fluorescence and second harmonic generation," Proc Natl Acad Sci U S A 100, 7075-7080 (2003).

[25] R. Carriles, D. N. Schafer, K. E. Sheetz, J. J. Field, R. Cisek, V. Barzda, A. W. Sylvester, and J. A. Squier, "Invited review article: Imaging techniques for harmonic and multiphoton absorption fluorescence microscopy," Rev Sci Instrum 80, 081101 (2009).

[26] N. Nishimura, C. B. Schaffer, B. Friedman, P. S. Tsai, P. D. Lyden, and D. Kleinfeld, "Targeted insult to subsurface cortical blood vessels using ultrashort laser pulses: three models of stroke," Nat Methods 3, 99-108 (2006).

[27] D. G. Ouzounov, T. Wang, M. Wang, D. D. Feng, N. G. Horton, J. C. Cruz-Hernandez, Y. T. Cheng, J. Reimer, A. S. Tolias, N. Nishimura, and C. Xu, "In vivo three-photon imaging of activity of GCaMP6-labeled neurons deep in intact mouse brain," Nat Methods 14, 388-390 (2017).

[28] N. Nishimura, C. B. Schaffer, B. Friedman, P. D. Lyden, and D. Kleinfeld, "Penetrating arterioles are a bottleneck in the perfusion of neocortex," Proc Natl Acad Sci U S A 104, 365-370 (2007).

[29] D. M. Small, W. Y. Sanchez, S. Roy, M. J. Hickey, and G. C. Gobe, "Multiphoton fluorescence microscopy of the live kidney in health and disease," J Biomed Opt 19, 020901 (2014).

[30] C. Auffray, D. Fogg, M. Garfa, G. Elain, O. Join-Lambert, S. Kayal, S. Sarnacki, A. Cumano, G. Lauvau, and F. Geissmann, "Monitoring of blood vessels and tissues by a population of monocytes with patrolling behavior," Science 317, 666-670 (2007).

[31] A. D. Aguirre, C. Vinegoni, M. Sebas, and R. Weissleder, "Intravital imaging of cardiac function at the single-cell level," Proc Natl Acad Sci U S A 111, 11257-11262 (2014).

[32] D. Debarre, W. Supatto, and E. Beaurepaire, "Structure sensitivity in third-harmonic generation microscopy," Opt Lett 30, 2134-2136 (2005).

[33] D. Debarre, W. Supatto, A. M. Pena, A. Fabre, T. Tordjmann, L. Combettes, M. C. Schanne-Klein, and E. Beaurepaire, "Imaging lipid bodies in cells and tissues using third-harmonic generation microscopy," Nat Methods 3, 47-53 (2006).

[34] G. Bautista, S. G. Pfisterer, M. J. Huttunen, S. Ranjan, K. Kanerva, E. Ikonen, and M. Kauranen, "Polarized THG microscopy identifies compositionally different lipid droplets in mammalian cells," Biophys J 107, 2230-2236 (2014).

[35] M. J. Farrar, F. W. Wise, J. R. Fetcho, and C. B. Schaffer, "In vivo imaging of myelin in the vertebrate central nervous system using third harmonic generation microscopy," Biophys J 100, 1362-1371 (2011).

[36] Y. C. Chen, H. C. Hsu, C. M. Lee, and C. K. Sun, "Third-harmonic generation susceptibility spectroscopy in free fatty acids," J Biomed Opt 20, 095013 (2015).

[37] M. Seeger, A. Karlas, D. Soliman, J. Pelisek, and V. Ntziachristos, "Multimodal optoacoustic and multiphoton microscopy of human carotid atheroma," Photoacoustics 4, 102-111 (2016).

[38] H. C. Stary, A. B. Chandler, S. Glagov, J. R. Guyton, W. Insull, Jr., M. E. Rosenfeld, S. A. Schaffer, C. J. Schwartz, W. D. Wagner, and R. W. Wissler, "A definition of initial, fatty streak, and intermediate lesions of atherosclerosis. A report from the Committee on Vascular Lesions of the Council on Arteriosclerosis, American Heart Association," Arterioscler Thromb 14, 840-856 (1994).

[39] K. S. Meir and E. Leitersdorf, "Atherosclerosis in the apolipoprotein-E-deficient mouse: a decade of progress," Arterioscler Thromb Vasc Biol 24, 1006-1014 (2004).

[40] D. A. Tulis, "Histological and morphometric analyses for rat carotid balloon injury model," Methods Mol Med 139, 31-66 (2007).

[41] N. G. Horton and C. Xu, "Dispersion compensation in three-photon fluorescence microscopy at 1,700 nm," Biomed Opt Express 6, 1392-1397 (2015).

[42] S. Lhotak, G. Gyulay, J. C. Cutz, A. Al-Hashimi, B. L. Trigatti, C. D. Richards, S. A. Igdoura, G. R. Steinberg, J. Bramson, K. Ask, and R. C. Austin, "Characterization of Proliferating Lesion-Resident Cells During All Stages of Atherosclerotic Growth," J Am Heart Assoc 5(2016).

[43] H. C. Stary, A. B. Chandler, R. E. Dinsmore, V. Fuster, S. Glagov, W. Insull, Jr., M. E. Rosenfeld, C. J. Schwartz, W. D. Wagner, and R. W. Wissler, "A definition of advanced types of atherosclerotic lesions and a histological classification of atherosclerosis. A report from the Committee on Vascular Lesions of the Council on Arteriosclerosis, American Heart Association," Arterioscler Thromb Vasc Biol 15, 1512-1531 (1995).

[44] R. Virmani, F. D. Kolodgie, A. P. Burke, A. Farb, and S. M. Schwartz, "Lessons from sudden coronary death: a comprehensive morphological classification scheme for atherosclerotic lesions," Arterioscler Thromb Vasc Biol 20, 1262-1275 (2000).

[45] Y. Nakashima, H. Fujii, S. Sumiyoshi, T. N. Wight, and K. Sueishi, "Early human atherosclerosis: accumulation of lipid and proteoglycans in intimal thickenings followed by macrophage infiltration," Arterioscler Thromb Vasc Biol 27, 1159-1165 (2007).

[46] A. J. Lusis, "Atherosclerosis," Nature 407, 233-241 (2000).

[47] J. L. Suhalim, C. Y. Chung, M. B. Lilledahl, R. S. Lim, M. Levi, B. J. Tromberg, and E. O. Potma, "Characterization of cholesterol crystals in atherosclerotic plaques using stimulated Raman scattering and second-harmonic generation microscopy," Biophys J 102, 1988-1995 (2012).

[48] H. N. Hutson, T. Marohl, M. Anderson, K. Eliceiri, P. Campagnola, and K. S. Masters, "Calcific Aortic Valve Disease Is Associated with Layer-Specific Alterations in Collagen Architecture," PLoS One 11, e0163858 (2016).

[49] L. M. Zadrozny, E. B. Neufeld, B. M. Lucotte, P. S. Connelly, Z. X. Yu, L. Dao, L. Y. Hsu, and R. S. Balaban, "Study of the development of the mouse thoracic aorta three-dimensional macromolecular structure using two-photon microscopy," J Histochem Cytochem 63, 8-21 (2015).

[50] W. Yu, J. C. Braz, A. M. Dutton, P. Prusakov, and M. Rekhter, "In vivo imaging of atherosclerotic plaques in apolipoprotein E deficient mice using nonlinear microscopy," J Biomed Opt 12, 054008 (2007).

[51] A. Zoumi, X. Lu, G. S. Kassab, and B. J. Tromberg, "Imaging coronary artery microstructure using second-harmonic and two-photon fluorescence microscopy," Biophys J 87, 2778-2786 (2004).

[52] R. S. Lim, A. Kratzer, N. P. Barry, S. Miyazaki-Anzai, M. Miyazaki, W. W. Mantulin, M. Levi, E. O. Potma, and B. J. Tromberg, "Multimodal CARS microscopy determination of the impact of diet on macrophage infiltration and lipid accumulation on plaque formation in ApoE-deficient mice," J Lipid Res 51, 1729-1737 (2010).

[53] R. Chevre, J. M. Gonzalez-Granado, R. T. Megens, V. Sreeramkumar, C. Silvestre-Roig, P. Molina-Sanchez, C. Weber, O. Soehnlein, A. Hidalgo, and V. Andres, "High-resolution imaging of intravascular atherogenic inflammation in live mice," Circ Res 114, 770-779 (2014).

[54] Z. Wu, A. Curaj, S. Fokong, E. A. Liehn, C. Weber, T. Lammers, F. Kiessling, and M. Zandvoort van, "Rhodamine-loaded intercellular adhesion molecule-1-targeted microbubbles for dual-modality imaging under controlled shear stresses," Circ Cardiovasc Imaging 6, 974-981 (2013).

[55] K. Arakawa, K. Isoda, T. Ito, K. Nakajima, T. Shibuya, and F. Ohsuzu, "Fluorescence analysis of biochemical constituents identifies atherosclerotic

plaque with a thin fibrous cap," Arterioscler Thromb Vasc Biol 22, 1002-1007 (2002).

[56] G. van Soest, E. Regar, T. P. Goderie, N. Gonzalo, S. Koljenovic, G. J. van Leenders, P. W. Serruys, and A. F. van der Steen, "Pitfalls in plaque characterization by OCT: image artifacts in native coronary arteries," JACC Cardiovasc Imaging 4, 810-813 (2011).

[57] G. J. Ughi, H. Wang, E. Gerbaud, J. A. Gardecki, A. M. Fard, E. Hamidi, P. Vacas-Jacques, M. Rosenberg, F. A. Jaffer, and G. J. Tearney, "Clinical Characterization of Coronary Atherosclerosis With Dual-Modality OCT and Near-Infrared Autofluorescence Imaging," JACC Cardiovasc Imaging 9, 1304-1314 (2016).

[58] T. Wang, A. McElroy, D. Halaney, D. Vela, E. Fung, S. Hossain, J. Phipps, B. Wang, B. Yin, M. D. Feldman, and T. E. Milner, "Dual-modality fiber-based OCT-TPL imaging system for simultaneous microstructural and molecular analysis of atherosclerotic plaques," Biomed Opt Express 6, 1665-1678 (2015).

[59] R. Turcotte, D. J. Rutledge, E. Belanger, D. Dill, W. B. Macklin, and D. C. Cote, "Intravital assessment of myelin molecular order with polarimetric multiphoton microscopy," Sci Rep 6, 31685 (2016).

[60] H. W. Wang, I. M. Langohr, M. Sturek, and J. X. Cheng, "Imaging and quantitative analysis of atherosclerotic lesions by CARS-based multimodal nonlinear optical microscopy," Arterioscler Thromb Vasc Biol 29, 1342-1348 (2009).

[61] A. Zumbusch, G. R. Holtom, and X. S. Xie, "Three-dimensional vibrational imaging by coherent anti-Stokes Raman scattering," Physical Review Letters 82, 4142-4145 (1999).

[62] J. X. Cheng and X. S. Xie, "Coherent Anti-Stokes Raman Scattering Microscopy: Instrumentation, Theory, and Applications," J Phys Chem B 108, 827-840 (2004).

[63] L. Marcu, J. A. Jo, Q. Fang, T. Papaioannou, T. Reil, J. H. Qiao, J. D. Baker, J. A. Freischlag, and M. C. Fishbein, "Detection of rupture-prone atherosclerotic plaques by time-resolved laser-induced fluorescence spectroscopy," Atherosclerosis 204, 156-164 (2009).

[64] J. A. Jo, Q. Fang, T. Papaioannou, J. H. Qiao, M. C. Fishbein, A. Dorafshar, T. Reil, D. Baker, J. Freischlag, and L. Marcu, "Novel methods of time-resolved fluorescence data analysis for in-vivo tissue characterization: application to atherosclerosis," Conf Proc IEEE Eng Med Biol Soc 2, 1372-1375 (2004).

[65] J. A. Jo, Q. Fang, T. Papaioannou, J. D. Baker, A. H. Dorafshar, T. Reil, J. H. Qiao, M. C. Fishbein, J. A. Freischlag, and L. Marcu, "Laguerre-based method for analysis of time-resolved fluorescence data: application to in-vivo characterization and diagnosis of atherosclerotic lesions," J Biomed Opt 11, 021004 (2006).

[66] T. Wang, D. Halaney, D. Ho, M. D. Feldman, and T. E. Milner, "Two-photon luminescence properties of gold nanorods," Biomed Opt Express 4, 584-595 (2013).

[67] T. Wang, A. McElroy, D. Halaney, D. Vela, E. Fung, S. Hossain, J. Phipps, B. Wang, B. Yin, M. D. Feldman, and T. E. Milner, "Detection of plaque structure and composition using OCT combined with two-photon luminescence (TPL) imaging," Lasers Surg Med 47, 485-494 (2015).

[68] T. Wang, J. J. Mancuso, S. M. Kazmi, J. Dwelle, V. Sapozhnikova, B. Willsey, L. L. Ma, J. Qiu, X. Li, A. K. Dunn, K. P. Johnston, M. D. Feldman, and T. E. Milner, "Combined two-photon luminescence microscopy and OCT for

macrophage detection in the hypercholesterolemic rabbit aorta using plasmonic gold nanorose," Lasers Surg Med 44, 49-59 (2012).

[69] T. T. Le, I. M. Langohr, M. J. Locker, M. Sturek, and J. X. Cheng, "Label-free molecular imaging of atherosclerotic lesions using multimodal nonlinear optical microscopy," J Biomed Opt 12, 054007 (2007).

[70] T. Meyer, M. Chemnitz, M. Baumgartl, T. Gottschall, T. Pascher, C. Matthaus, B. F. Romeike, B. R. Brehm, J. Limpert, A. Tunnermann, M. Schmitt, B. Dietzek, and J. Popp, "Expanding multimodal microscopy by high spectral resolution coherent anti-Stokes Raman scattering imaging for clinical disease diagnostics," Anal Chem 85, 6703-6715 (2013).

[71] E. V. Gubarkova, V. V. Dudenkova, F. I. Feldchtein, L. B. Timofeeva, E. B. Kiseleva, S. S. Kuznetsov, B. E. Shakhov, A. A. Moiseev, V. M. Gelikonov, G. V. Gelikonov, A. Vitkin, and N. D. Gladkova, "Multi-modal optical imaging characterization of atherosclerotic plaques," J Biophotonics 9, 1009-1020 (2016).

[72] N. G. Horton, K. Wang, D. Kobat, C. G. Clark, F. W. Wise, C. B. Schaffer, and C. Xu, "three-photon microscopy of subcortical structures within an intact mouse brain," Nat Photonics 7(2013).

[73] D. Kobat, N. G. Horton, and C. Xu, "In vivo two-photon microscopy to 1.6-mm depth in mouse cortex," J Biomed Opt 16, 106014 (2011).

[74] C. Xu and F. W. Wise, "Recent Advances in Fiber Lasers for Nonlinear Microscopy," Nat Photonics 7(2013).

[75] D. Sinefeld, H. P. Paudel, D. G. Ouzounov, T. G. Bifano, and C. Xu, "Adaptive optics in multiphoton microscopy: comparison of two, three and four photon fluorescence," Opt Express 23, 31472-31483 (2015).

[76] N. Ji, "Adaptive optical fluorescence microscopy," Nat Methods 14, 374-380 (2017).

[77] S. H. Chia, C. H. Yu, C. H. Lin, N. C. Cheng, T. M. Liu, M. C. Chan, I. H. Chen, and C. K. Sun, "Miniaturized video-rate epi-third-harmonic-generation fiber-microscope," Opt Express 18, 17382-17391 (2010).

[78] C. L. Hoy, O. Ferhanoglu, M. Yildirim, W. Piyawattanametha, H. Ra, O. Solgaard, and A. Ben-Yakar, "Optical design and imaging performance testing of a 9.6-mm diameter femtosecond laser microsurgery probe," Opt Express 19, 10536-10552 (2011).

[79] D. M. Huland, K. Charan, D. G. Ouzounov, J. S. Jones, N. Nishimura, and C. Xu, "Three-photon excited fluorescence imaging of unstained tissue using a GRIN lens endoscope," Biomed Opt Express 4, 652-658 (2013).

[80] C. M. Brown, D. R. Rivera, I. Pavlova, D. G. Ouzounov, W. O. Williams, S. Mohanan, W. W. Webb, and C. Xu, "In vivo imaging of unstained tissues using a compact and flexible multiphoton microendoscope," J Biomed Opt 17, 040505 (2012).

CHAPTER 3

IN VIVO CALCIUM IMAGING OF CARDIOMYOCYTES IN THE BEATING MOUSE HEART WITH MULTIPHOTON MICROSCOPY

3.1 Introduction

Cardiovascular disease remains a substantial burden to populations worldwide (Mortality and Causes of Death, 2015; Mozaffarian et al., 2015). Despite significant advances in cardiovascular research, understanding of cell and tissue dynamics at a microscopic scale in vivo is lacking. Multiphoton microscopy (MPM) was recently demonstrated in the heart of live rodent models (Lee et al., 2012; Li et al., 2012; Jung et al., 2013; Aguirre et al., 2014; Vinegoni et al., 2015a; Vinegoni et al., 2015b). However, the combined use of intravital MPM and genetically encoded calcium indicators, which revolutionized recording of neurons (Pologruto et al., 2004; Chen et al., 2013; Prevedel et al., 2016), has not been achieved in the in vivo, beating heart. As a result, little is known about the interplay of in vivo microenvironmental features such as the microcirculation, motion, and other cellular factors which couple and modulate function of cardiomyocytes (Rubart et al., 2003b; Wasserstrom et al., 2010; Pries and Reglin, 2017). Better understanding of the interactions between cell contraction, blood flow, and electrical conduction in disease is also needed. Previous in vivo studies of calcium dynamics utilized wide-field fluorescence imaging that primarily reports surface calcium transients averaged across many cells (Tallini et al., 2006; Jaimes et al., 2016). At the single-cell level, intracellular myocyte calcium and voltage transients (Rubart et al., 2003b; Wasserstrom et al., 2010; Ghouri et al., 2015), calcium dynamics of cells transplanted into myocardium (Rubart et al., 2003a; Rubart et al., 2004; Scherschel et al., 2008; Smart et al., 2011), differences that occur with pathological hypertrophy (Tao et al., 2012), and triggered arrhythmias (Fujiwara et al.,

2008) have been characterized in noncontracting Langendorff-perfusions. However, altered electromechanical function and inadequate oxygenation can drastically affect measurements of physiology in such perfused heart preparations (Kuzmiak-Glancy et

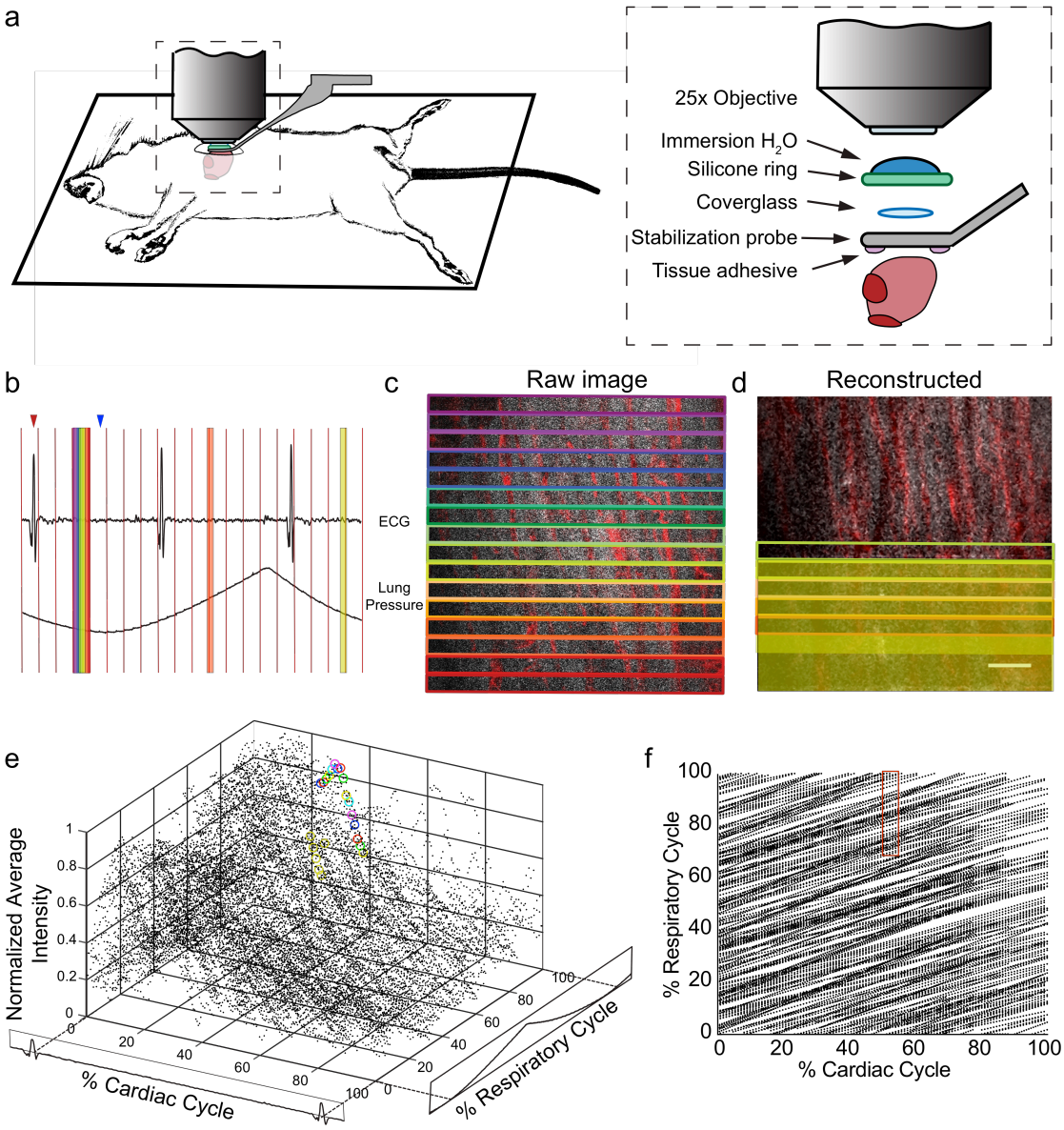

Figure 7. Combination of surgical approach and image reconstruction methods enable visualization and quantification of cardiac cell dynamics. (a) Optical access is gained via a left thoracotomy and a stabilization probe is attached to the left ventricle for microscopy. The probe holds a 3-mm diameter coverglass in contact with the heart. A silicone ring is glued to the top of the probe to hold water for the immersion of the microscope objective. Tissue adhesive is applied on the bottom surface of the probe prior to attachment to the heart. (b) Electrocardiogram (ECG) and ventilator pressure are recorded simultaneously during image acquisition allowing

image reconstruction. Red vertical lines indicate the start of each frame; red arrow indicates the peak of R-wave used as the start of the cardiac cycle for the frame displayed below; blue arrow indicates the start of inhalation that was used as the marker of respiratory cycle; yellow box indicates 5% binning window (35-40% of cardiac cycle) used in the reconstructed frame shown in d, data from the red box was not included in reconstructed frame due to its vicinity to the peak pressure of the ventilator. (c) Single raw image frames with colored boxes indicating the image segments, with corresponding timing of the acquisition indicated on the ECG and ventilator pressure traces, the yellow box highlights image segments used in the example reconstructed image shown in d. (d) A plane reconstructed using 512x33 pixel segments, 5% of the cardiac cycle, restricted to 70-100% of the respiratory cycle, and averaged across 4 μm in z. In c and d, GCaMP6f signal is shown in grey, and vasculature is shown in red. Scale bar indicates 50 μm. (e) GCaMP6f signal as a function of cardiac and respiratory cycles. Each data point is the intensity averaged in a 512x33-pixel segment with values normalized to the maximum intensity per axial slice. 50 frames acquired per z-plane, spanning 90 μm in z. Circled points correspond to data taken from regions outlined in corresponding colors in the raw image frame in c. (f) Data density in the 2D parameter space. Each point represents a 512x33-pixel segment from the raw image data. The red box indicates portion of the cardiac and respiratory cycle used to generate the reconstructed plane d.

al., 2015). The elimination of motion and blood flow results in highly artificial conditions and also precludes studies of the correlation between local vascular and tissue function possible in other tissues such as the brain (Shih et al., 2012; Cianchetti et al., 2013).

Here, we demonstrate MPM imaging of the genetically encoded calcium indicator GCaMP6f (Chen et al., 2013) in the beating heart within a living mouse. We show the capability to resolve calcium dynamics in single cardiomyocytes and characterize the dependence of the calcium signal on both cardiac and respiratory cycles as well as depth. Previous methods needed to compromise by limiting measurements to points in the cardiac and respiratory cycle when motion was minimized, resulting in a restricted measure of function. Our methods can measure local contraction, excitation, and vascular changes all with microscopic resolution without breath holds throughout the cardiac cycle.

3.2 Materials and methods

3.2.1 Animals

Mice expressing the Cre-dependent GCaMP6f fast variant calcium indicator gene (B6;129S-Gt(ROSA)26Sortm95.1(CAG-GCaMP6f)Hze/J - Jackson Labs; #024105) (Chen et al., 2013) were bred on site with B6.Cg-Tg(CAG-cre/Esr1*)5Amc/J (CAG-cre/Esr1) mice (Jackson Labs; #004682) (Hayashi and McMahon, 2002). Expression of GCaMP6f was induced by intraperitoneal injection of tamoxifen in corn oil (Sigma #T5648) for 5 consecutive days (75 mg/kg body weight), resulting in widespread tissue expression with strong expression in cardiomyocytes. C57BL/6 wild-type mice were used for control experiments. Male and female mice (25 – 40 g), aged 4 – 10 months old were used for experiments. This study was carried out in accordance with the recommendations of Guide for the Care and Use of Laboratory Animals by the National Institutes of Health. The protocol was approved by the Institutional Animal Care and Use Committee of Cornell University.

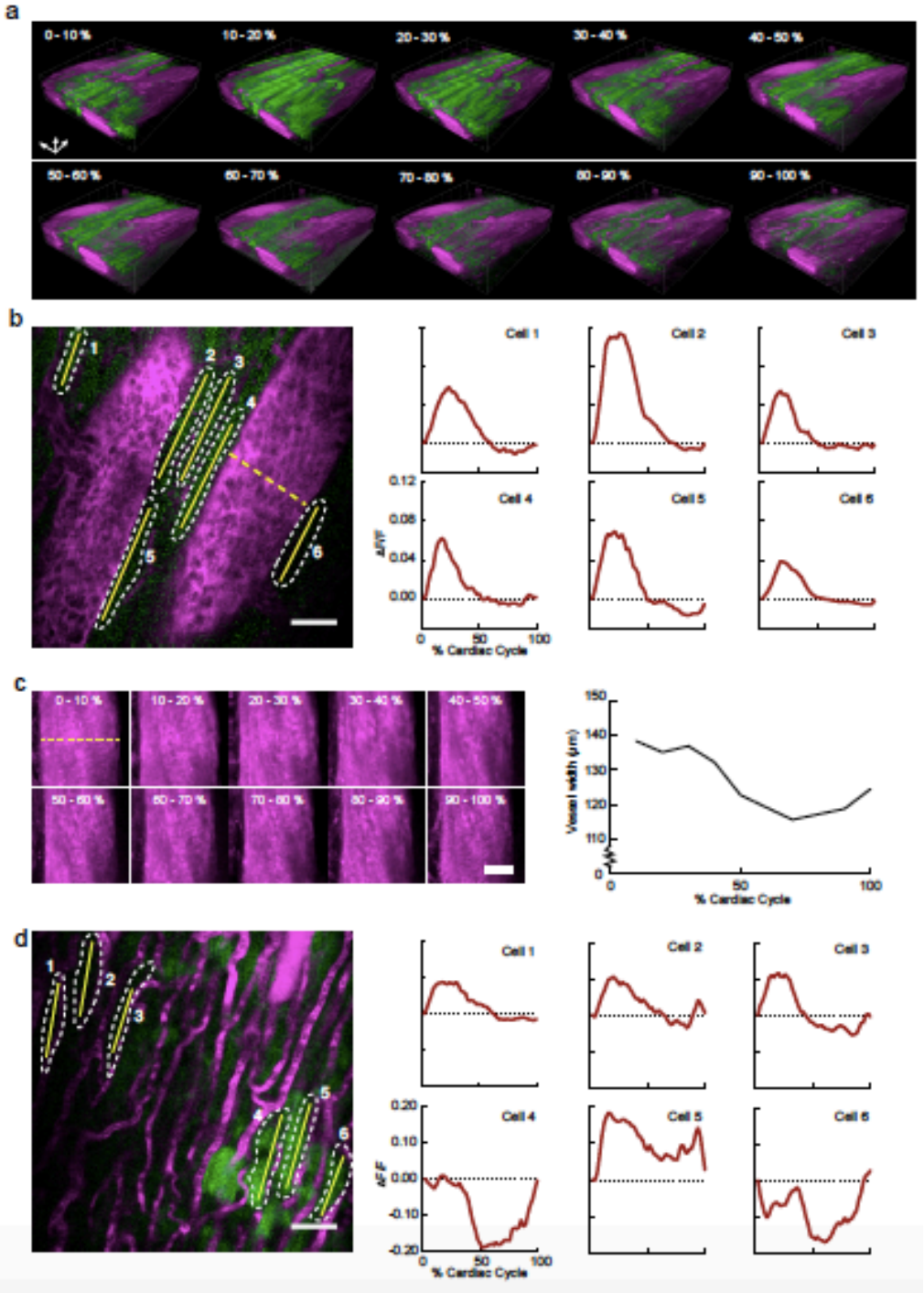

Figure 8. Volumetric image reconstruction enables quantification of collective and single-cell activity in the heart. (a) 3D renderings of image volumes reconstructed from segments of 512 x 33 pixels, at the indicated cardiac cycle phases, including 50-100% of the respiratory cycle. (b) GCaMP6f intensity change (ΔF/F0) in six individual cardiomyocytes (shown in a single raw image) throughout the cardiac cycle. Quantitative traces were taken from images reconstructed with 512 x 33 pixels segments, 2% of the cardiac cycle, including 50-100% of the respiratory cycle, and

averaged over 14 μm in depth. (c) Change in vessel width over the cardiac cycle from the same imaged volume (indicated by dashed yellow line in b). Images show z-axis maximum intensity projections of images reconstructed from 512 x 33 pixel segments, averaged over 10% of cardiac cycle, including 50-100 % of the respiratory cycle. (d) Single raw image and fluorescence changes from cells in a region near laser-induced sterile injury. Images were reconstructed as in b for quantitative analysis. GCaMP6f channel is shown in green, and Texas-Red dextran shows vasculature in magenta. All scale bars indicate 50 μm.

3.2.2 Design of stabilization window and surgery for imaging

The design of the stabilization window and imaging setup is shown in Fig. 7a and b and Supple. Fig.1. The probe is composed of 3D-printed titanium (iMaterialize, Belgium) with a 2-mm central aperture that accepts a 3-mm diameter coverslip (Deckglaser Cover Glasses, 64-0726 #0). The tissue interface side of the probe was sanded and a channel was etched around the central aperture using fs laser ablation with 1-kHz, 15-μJ, 800-nm, 50-fs laser pulses, translated at 0.1 mm/s and focused with a 0.28 NA microscope objective (Cerami et al., 2013). This channel prevents tissue adhesive spilling underneath the coverslip and impairing image quality. A silicone ring, fashioned from silicone molding putty (Castaldo Qick-Sil), is adhered with Loctite-406 to the top side of the window to hold water for immersion of the microscope objective at the appropriate working distance. The tail of the probe is fixed to a micromanipulator that can translate the height of the window to facilitate placement onto the ventricle wall, and provide an anchorage point for stabilization during imaging.

3.2.3 Surgical preparation

Mice were anesthetized with ketamine (10 mg/mL) and xylazine (1 mg/mL) in saline via intraperitoneal injection (0.1 mL/10g body weight) and then intubated via the trachea using a 22-gauge, 1-inch catheter to allow mechanical ventilation (95 breath/min, 12 cm H2O end-inspiratory pressure; CWE Inc. SAR-830/P ventilator)

with medical grade oxygen and 1.5% isoflurane for maintaining anesthesia. The ventilation rate was selected for optimum animal stability and also to avoid harmonics of the heart rate so that the cardiac and respiratory cycles were out of phase. The mouse was positioned on its right side, on top of a motorized stage with a heating pad to maintain body temperature at 37.5 ºC. Hair over the left thorax was depilated, skin and muscle layers over the chest wall excised, and the intercostal space between ribs 7 and 8 perforated and retracted to create space for placement of the window. Following removal of the pericardial sac, the stabilization probe was attached to the left ventricle free-wall using tissue adhesive (Vetbond). Tissue adhesive was applied to the underside of the probe and the window was gently lowered onto the left ventricle wall. A two translational-axis micromanipulator, mounted on the surgical stereotaxic holding the animal, provided stabilization and positioning of the probe (Fig. 7 and Fig. 13). ECG electrodes were attached to 21 gauge needles inserted subcutaneously through the front and contralateral hind limb, connected through an isolated differential amplifier (World Precision Instruments; #ISO-80), and recorded inside a Faraday enclosure mounted to the microscope. ECG and ventilation pressure (from ventilator) signals were continuously monitored on an oscilloscope and recorded simultaneously with image acquisition. 5% glucose in saline (0.1 mL/10 g body weight) and 0.15 mg/mL atropine sulfate (5 µg/100 g body weight) were injected subcutaneously every 30 min throughout surgery and in vivo microscopy. This procedure allowed stable in vivo imaging for 1 h. A retro-orbital injection of Texas-Red conjugated, 70 kDa dextran (3% in saline; Thermo #D1830) was performed to label blood plasma providing contrast in the vasculature.

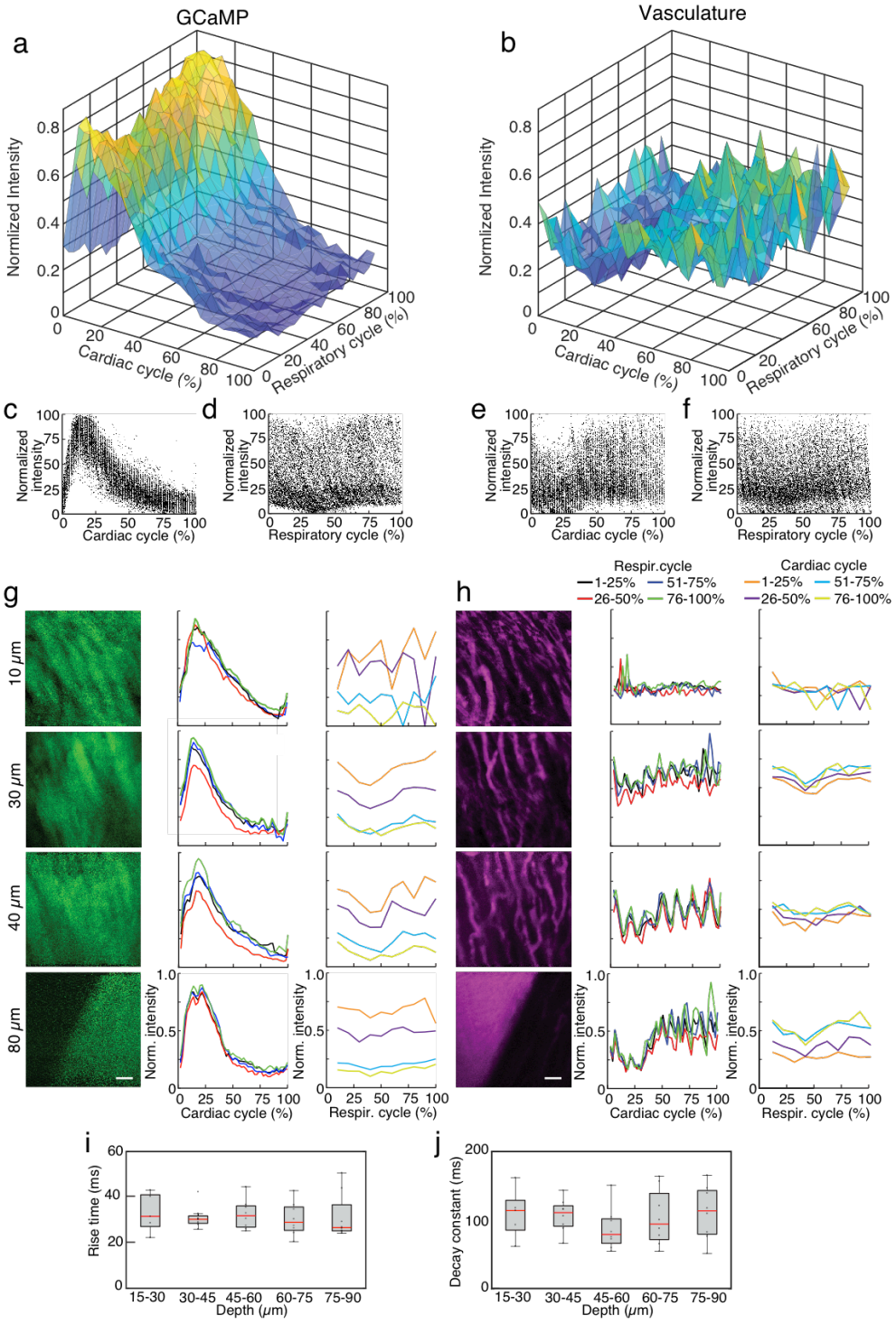

Figure 9. GCaMP6f imaging in ventricle wall. (a) Intensity of the calcium indicator GCaMP6f and (b) Texas-Red fluorescence channels as a function of cardiac and respiratory cycle averaged over a stack spanning 90 μm in depth. Displayed values are

the average intensities from 512 x 33 pixel segments, normalized to the maximum intensity in the sequential series of raw images acquired at that plane. Data were combined in bins of 25% of both cardiac and respiratory cycle. Plots of the same data showing all individual measurements of GCaMP6f intensity across (c) cardiac and (d) respiratory cycles and from the Texas-Red channel across (e) cardiac and (f) respiratory cycles. (g) GCaMP6f channel and (h) Texas-Red channel reconstructed image projections (left), average plots of fluorescence intensities as function of cardiac phase (middle) and respiratory phase (right). Images include 50-100% of respiratory cycle, and bin 10% of the cardiac cycle, and include 10 μm in z. The cardiac dependence (middle) used bins of 2% of the cardiac cycle. The respiratory dependence used bins of 10% of the respiratory cycle. Color of lines indicate phase range of trace in opposing cycle. Scale bars are 50 μm.

3.2.4 In vivo cardiac multiphoton microscopy

Imaging was conducted using a custom multiphoton microscope equipped with four detection channels and an 8-kHz resonant scanner (Cambridge Technology) imaged onto a galvanometric pair (Cambridge Technology) to allow for both resonant and line scanning. Resonant scanning data acquisition was performed using a National Instruments digitizer (NI-5734), FPGA (PXIe-7975), and multifunction I/O module (PXIe-6366) for device control, mounted in a PXI chassis (PXIe-1073) controlled by ScanImage 2016b (Pologruto et al., 2003). A Ti:Sapph laser (Chameleon, Coherent) with the wavelength centered at 950 nm, was used to simultaneously excite GCaMP6f and Texas-Red fluorescence. Emission was separated using a primary dichroic (Semrock FF705-Di01-49x70), a secondary dichroic (Semrock FF593-Di03-90x108), and bandpass filters selective for GCaMP6f (517/65) and Texas-Red (629/56). Water was placed within the silicone O-ring of the stabilization probe to immerse the microscope objective (Olympus XLPlan N 25x 1.05 NA). Z-stack images were collected to a depth of 100–150 μm from the surface (2 μm per z-step) at 4–5 different locations per mouse. A series of 50–100 frames (1.7 to 3.3 s) per plane in z were collected at a scan speed of 30 frame/sec.

3.2.5 Assigning cardiac and respiratory phase to image segments

The R-wave and expiration peaks were found using *findpeak* from the Matlab Signal Processing Toolbox to generate a lookup table for cardiorespiratory-dependent image

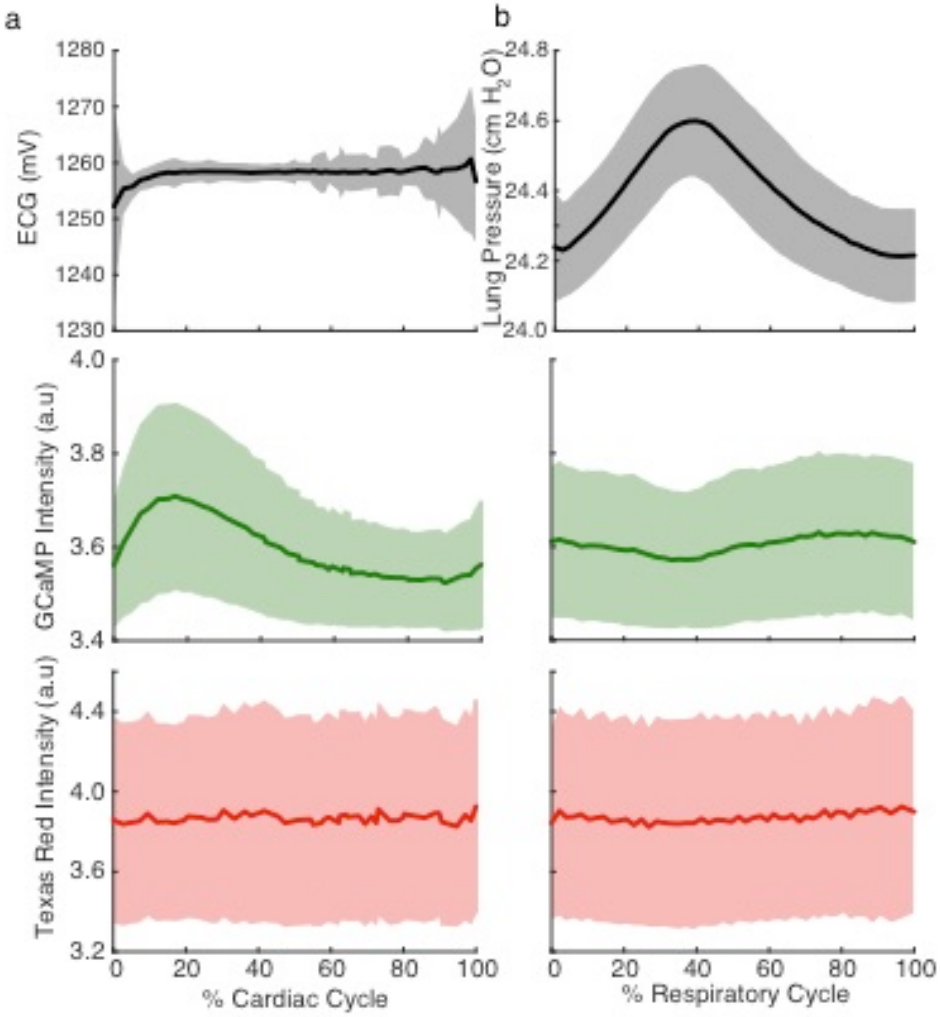

Figure 10. Cardiac and respiratory cycle variation in fluorescence. (a) Electrocardiogram voltage (ECG), fluorescence from GCaMP6f and Texas Red injected in vasculature as a function of phase in cardiac cycle. All phases of respiratory cycle were included. (b) Ventilator pressure, and GCaMP6f and Texas Red signal as a function of phase in respiratory cycle. All phases of the cardiac cycle were included. Solid line shows mean and shading shows standard deviation from eight stacks in three animals. (c) Rise time and (d) decay constants from the calcium responses from ten regions of interest across three animals (2% bins of the cardiac cycle, excluded 25-50% of the respiratory cycle, and binned 15 μm in depth). Box edges represent 25th and 75th percentiles, box centerline indicates median, and whiskers are most extreme data not considered outlier. Open circles show means. ANOVA showed no significant differences in groups ($p = 0.67$, $p = 0.97$).

reconstruction and quantification. We found that with a heart rate of approximately 5 Hz and breathing at 2 Hz, ~1.5 seconds or about 50 frames was sufficient to generate images in most of the cardiac/respiratory cycle space. Raw images were divided into segments of n_{block} lines in the fast-scan axis (x) direction. Because the scan rate in x-direction (0.058 ms per line) is fast compared to the dynamics of the cardiac cell, we assigned image segments a single value of time relative to heartbeat and breathing. For all image segments, a look-up table was generated with position in y, position in z, time relative to the preceding R wave, time relative to the preceding trough of lung pressure, average intensity value, and a unique identifier of each heartbeat, which were used for calcium transient and image reconstruction. Phase in cardiac cycle was defined as

$$Cardiac\ cycle\ phase = \frac{t_{seg} - R_{time_1}}{max_z(R_{time_2} - R_{time_1})}$$

and phase in respiratory cycle was defined as

$$Respiratoy\ cycle\ phase = \frac{t_{seg} - E_{time_1}}{max_z(E_{time_2} - E_{time_1})}$$

where t_{seg} is the time of a given segment, R_{time_1} is the time of the preceding R wave, R_{time_2} is the time of the following R wave, E_{time_1} is the time of the preceding trough of pressure, E_{time_2} is the time of the following trough of pressure, and max_z is the maximum occurring at a given z position. For exclusion of vascular regions in the quantification of fluorescence, the cardiomyocytes were identified by manually setting intensity thresholds to extracellular regions.

3.2.6 Reconstruction of image stack

Image planes and volumes are reconstructed by sorting segments in the cardiorespiratory cycle. Each image segment within a selected range of the cardiorespiratory cycle was then registered by the position in y and z into a reconstructed stack. In cases where more than one image segment registered to the

same position in the reconstruction, the redundant data was averaged. In many applications, segments with a range of z-positions can be averaged together if the loss in spatial resolution is acceptable. The choice of segment size, and binning in the cardiac and respiratory cycles affect the temporal and spatial resolution of the method. The binning parameters and the amount of data acquired should be varied to fit the needs of the experiment and are reported here for each set of data presented in the figures.

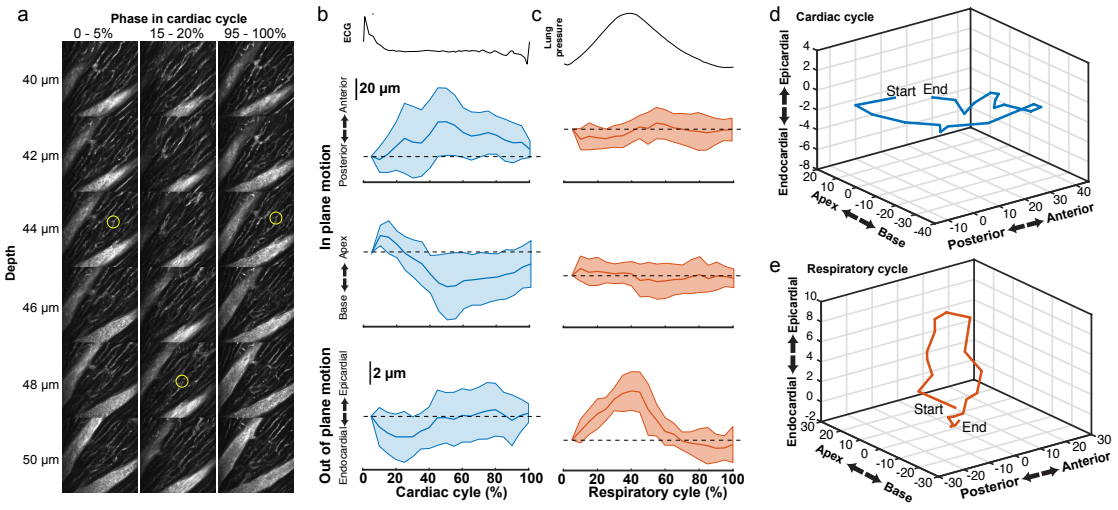

Figure 11. Tissue motion throughout cardiac cycle. (a) Representative images of myocardial vasculature labelled with Texas-Red dextran dye used for tracking the 3D motion of a structure (yellow circle) at the indicated phases in the cardiac cycle. Reconstruction used 512 x 65 pixel segments, 5% cardiac cycle bins, included 50-100% of respiratory cycle and used 2-µm bins in z. (b) Average change in the position of features in the myocardium throughout the cardiac cycle from reconstructions from and (c) throughout the respiratory cycle (from same data, reconstructed including data 50–100% of the cardiac cycle, 5% respiratory bins). Solid lines are average and shading indicates standard deviation from 14 measurements from eight stacks in three animals. (d) Three-dimensional average trajectory of the same data showing the average displacement due to cardiac and (e) respiratory motion.

3.2.7 Calculation of rise time and tau

Intensity values from stacks were averaged over 15 µm in depth. To eliminate non-calcium dependent signals coming from autofluorescence, data from the top 15-30 µm

of the raw image stack was not included so that the analysis used only frames with visible calcium transients. Due to the drop in fluorescent signal associated with inspiration, data from 25-50% of the respiratory cycle was excluded. Intensity was binned across 2% of the cardiac cycle and normalized to the maximum intensity in the series of images acquired at a particular depth. A single term exponential curve was fit from 90% of the peak intensity of the transient to the minimum for calculation of tau (Hammer et al., 2014). The average time from the R wave to the maximum value of the transient was used for the rise time.

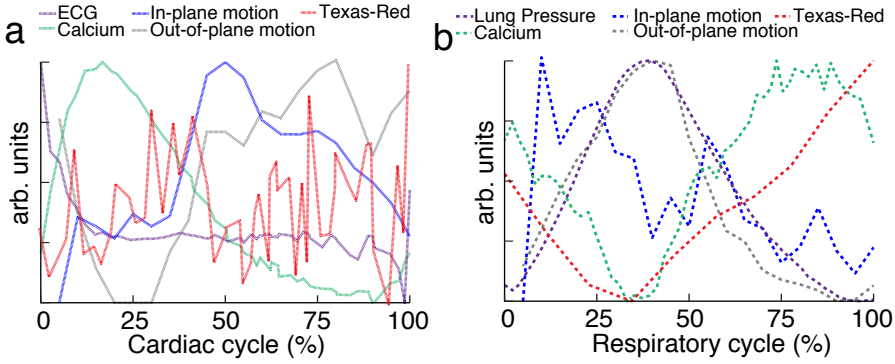

Figure 12. Relative timing of measured dynamics. (a) Summary of mean trends as a function of cardiac and (b) respiratory phase. In-plane motion, is calculated as from means in Figure 5 as $\sqrt{x^2 + y^2}$. All curves have been normalized to the maximum and minimum.

3.2.8 Image display and rendering

Intensity values from stacks were averaged over 15 µm in depth. To eliminate non-calcium dependent signals coming from autofluorescence, data from the top 15-30 µm of the raw image stack was not included so that the analysis used only frames with visible calcium transients. Due to the drop in fluorescent signal associated with inspiration, data from 25-50% of the respiratory cycle was excluded. Intensity was binned across 2% of the cardiac cycle and normalized to the maximum intensity in the series of images acquired at a particular depth. A single term exponential curve was fit from 90% of the peak intensity of the transient to the minimum for calculation of

tau (Hammer et al., 2014). The average time from the R wave to the maximum value of the transient was used for the rise time.

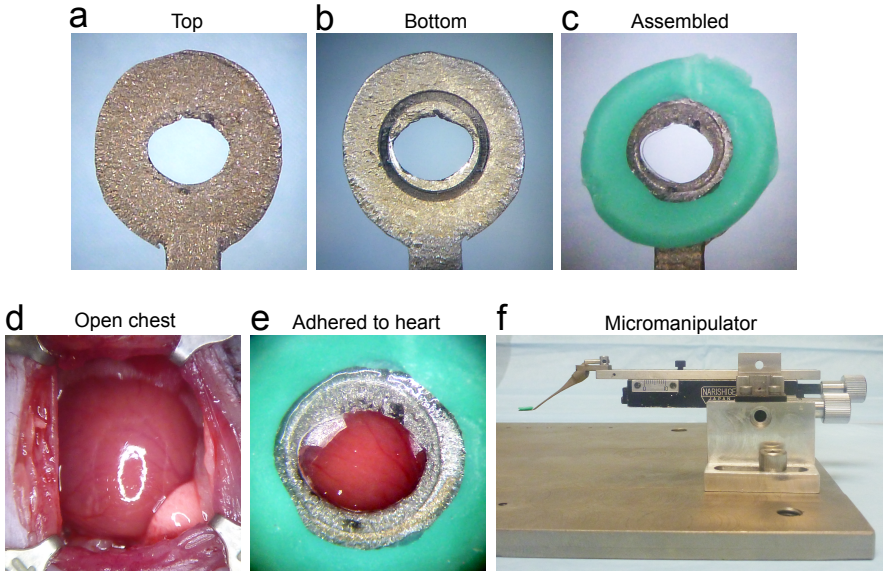

Figure 13. Stabilization probe. (a) top and (b) bottom views of the 3D-printed titanium stabilization probe. A femtosecond laser ablated groove on the underside that prevents tissue adhesion from leaking underneath the coverglass. (c) Assembled probe containing the 3-mm diameter coverglass and green silicone ring that serves as reservoir for the microscope objective immersion fluid. (d) Left side thoracotomy of the mouse presents the left ventricular wall for placement of the imaging window. (e) Probe attached to the heart showing the left ventricle myocardium through the imaging. (f) Stabilization probe attached to the micromanipulator which allows accurate placement of the probe onto the ventricle wall.

3.2.9 Single-point motion tracking

ImageJ (imagej.nih.gov/ij) was used to display and process reconstructed images. A median filter (1 pixel) was applied and contrast adjusted for display using only linear scaling. When displaying changes in intensity of GCaMP6f, the displayed range of values was the same at each time point. Renderings of 3D stacks were produced using Imaris x64 version 9.0.2 (Bitplane). The blend mode in Imaris was used to display the volume following the application of a smoothing filter (3 x 3 x 1 pixel size).

To quantify motion in the myocardium due to cardiac contraction, images were reconstructed by averaging over 5% of the cardiac cycle time, only using images

captured during 50–100% of the respiratory cycle. To quantify motion in the myocardium due to respiratory movement, images were reconstructed averaging over 5% of the respiratory cycle, only using images captured during 50–100% of the cardiac cycle. Both cardiac and respiratory cycle reconstructions used 65 x 512 segments of each frame. ImageJ was used to display reconstructed stacks combined at each 2 µm depth, with each frame of the stack representing sequential 0–5% averaged images throughout the cardiac or respiratory cycle. This allows the point of a small vessel bifurcation to be tracked throughout each 0–5% averaged increment of the cycle and each position (x, y, z) to be recorded. These measurements were repeated across three mice consisting of a total of 8 image stacks and of 14 tracked single points.

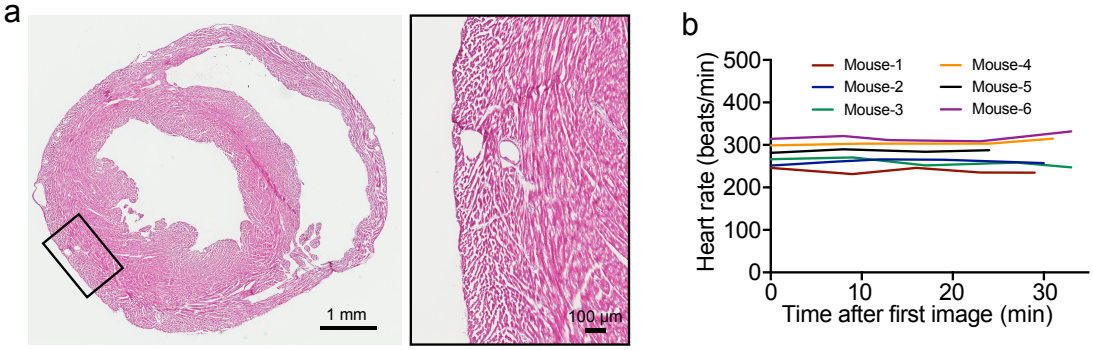

Figure 14. Histology of the imaged heart. (a) Hematoxylin and eosin staining of in vivo, MPM imaged heart demonstrated no observable damage to cell structure (insert). (b) Heart rate during imaging remains constant.

3.2.10 Single-cell calcium quantification

To quantify cardiomyocyte calcium transients, images were reconstructed from 512 x 33 pixel segments, averaging over 2% of the cardiac cycle, using images captured during 50-100% of the respiratory cycle. Reconstructed images were averaged over 14 µm in z, to account for motion in z due to the cardiac cycle. ImageJ was used to draw a line along the longitudinal axis of a cardiomyocyte within the bounds of the vasculature and provide a mean intensity value at each 2% of the cardiac cycle. The

ΔF/F (ΔF, fluorescence intensity change from fluorescence at R wave; F, fluorescence intensity at R wave) was calculated and filtered using the filter function in Matlab with a window size of 5 and periodic boundary conditions.

3.2.11 Vessel width quantification

To quantify changes in vessel diameter, images were reconstructed using 512 x 33 pixel segments, averaging over 10% of the cardiac cycle time, using images captured during 50-100% of the respiratory cycle. Z-slices were maximum intensity projected in the z-axis to produce a single frame that was rotated so that the vessel was vertical. The line tool in ImageJ was used to take 5 measurements of the vessel width at 10% increments in the phase of the cardiac cycle.

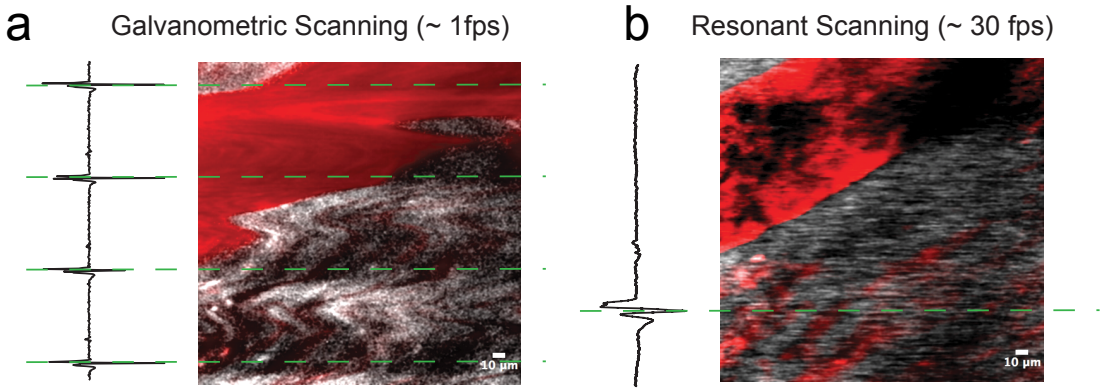

Figure 15. Higher frame rate imaging shows reduced in-frame motion due to heart contraction. Raw image frames showing same cardiac vessel with (a) standard galvonometric scanning and (b) resonant scanning. Green dotted lines indicate the timing of the peak of the R-wave from the electrocardiogram which align with image artifacts. Scale bar is 10 µm.

3.2.12 Software and code

Matlab was used for reconstruction and cardiorespiratory cycle-dependent analysis. Scripts are available in Supplementary Materials. Matlab was used for box plots and statistics analysis. Graphpad Prism 7 was used to generate graphs of single-cell calcium traces.

3.2.13 Histology

At the end of imaging, the probe was removed and the animal deeply anesthetized, followed by transcardial perfusion with cold (4°C) phosphate buffered saline (PBS, pH 7.4, Sigma-Aldrich) followed by 4% (w/v) paraformaldehyde (PFA, ThermoFisher Scientific) in PBS. The heart was excised and cut in the cross-sectional plane at the location of attached probe which was indicated by remnants of tissue adhesive. Hearts were placed in 4% PFA for 1 day, and then in 30% sucrose (w/v) in PBS for 1 day. The heart was frozen in Optimal Cutting Temperature (OCT) compound (Tissue-Tek) and cryo-sectioned at 7-µm thickness onto glass slides. Hematoxylin and eosin staining was performed using standard procedures.

3.3 Results

3.3.1 Surgical stabilization, fast scanning, and sorting by cardiac and respiratory phase enable in vivo MPM of cardiac dynamics

In anesthetized, mechanically ventilated mice, we acquired ~100-µm thick image stacks with 2-µm step size and 50-100 images per plane through a window mounted to a stabilized probe glued to the left ventricle (Fig. 7a, Fig. 13) while recording the ECG and ventilator pressure (Fig. 7b). This preparation caused no observable damage (Fig. 14a) and heart rate was stable throughout the imaging session (Fig. 14b). High frame rate imaging (30 fps), using resonant scanners, produced images in real time throughout the cardiac cycle, with minimal image distortion due to tissue motion as compared to slower scanning (Fig. 15). In contrast to previous approaches (Aguirre et al., 2014; Vinegoni et al., 2015b), breathing was not paused during measurement and image acquisition, and the heartbeat was not synchronized to acquisition. Instead, the effects of breathing and heartbeat were decoupled by reconstructing 3D volumes from smaller image segments sorted by both the cardiac and respiratory phase (Santisakultarm et al., 2012) (Fig. 7c-f), with the size of bins in phase and position in z adjusted for the needs of the application.

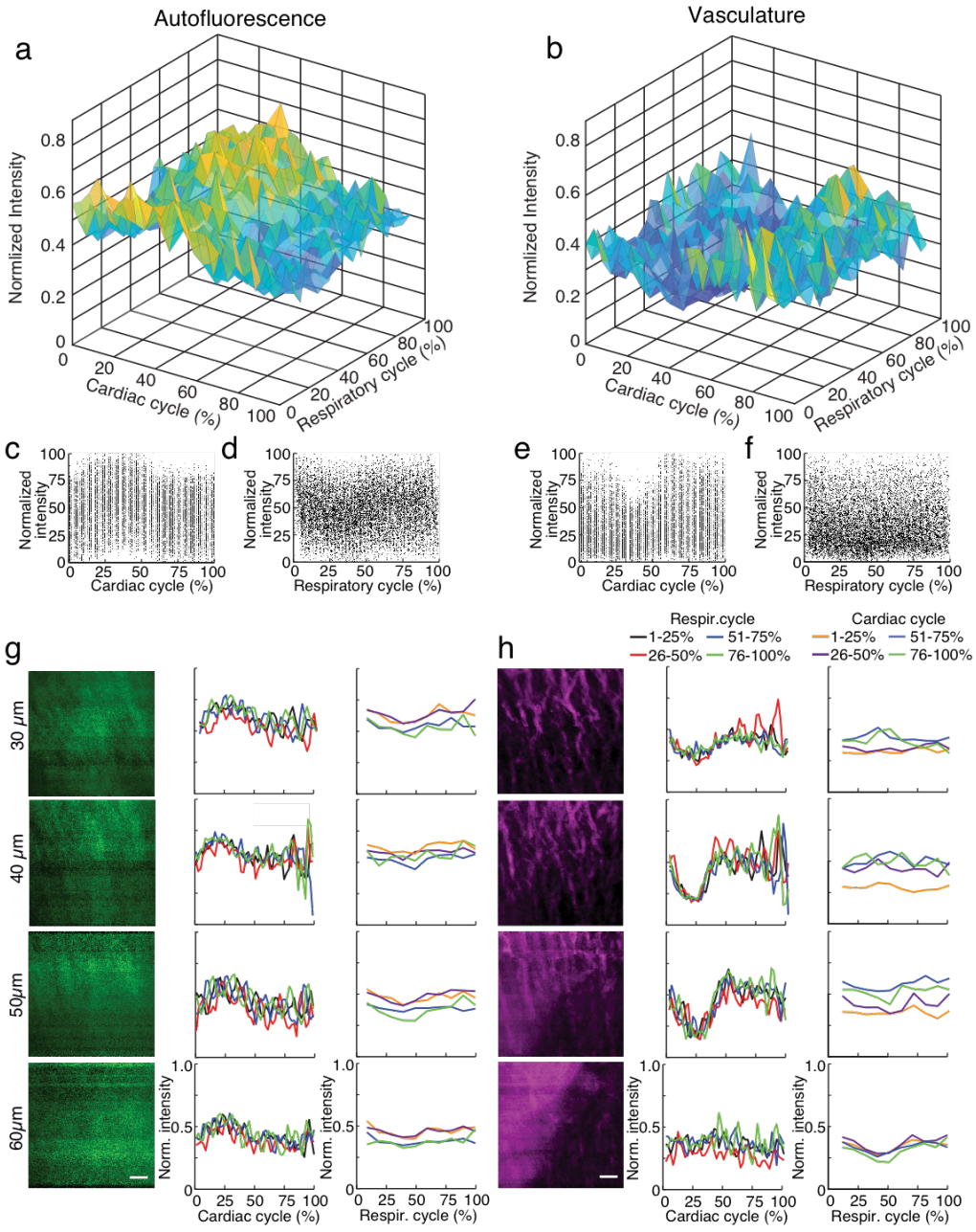

Figure 16. GCaMP6f imaging in ventricle wall. (a) Intensity of the calcium indicator GCaMP6f and (b) Texas-Red fluorescence channels as a function of cardiac and respiratory cycle averaged over a stack spanning 90 μm in depth. Displayed values are the average intensities from 512 x 33 pixel segments, normalized to the maximum intensity in the sequential series of raw images acquired at that plane. Data were combined in bins of 25% of both cardiac and respiratory cycle. Plots of the same

data showing all individual measurements of GCaMP6f intensity across (c) cardiac and (d) respiratory cycles and from the Texas-Red channel across (e) cardiac and (f) respiratory cycles. (g) GCaMP6f channel and (h) Texas-Red channel reconstructed image projections (left), average plots of fluorescence intensities as function of cardiac phase (middle) and respiratory phase (right). Images include 50-100% of respiratory cycle, and bin 10% of the cardiac cycle, and include 10 μm in z. The cardiac dependence (middle) used bins of 2% of the cardiac cycle. The respiratory dependence used bins of 10% of the respiratory cycle. Color of lines indicate phase range of trace in opposing cycle. Scale bars are 50 μm.

3.3.2 Volumetric image reconstruction shows both regional and single cell cardiomyocyte calcium transients in vivo

Reconstructed 3D stacks from a mouse expressing GCaMP6f in cardiomyocytes and with a vascular injection of dye enabled the clear visualization of blood vessels and cardiomyocytes and revealed the dynamic relationship throughout each phase of the cardiac cycle (Fig. 8a). Red blood cells were visible as dark patches within the fluorescent blood plasma in the vessel lumen (Kleinfeld et al., 1998). GCaMP6f intensity changes peaked at 10-20% of the cardiac cycle. Reconstructed single frame images from the same volume enabled the GCaMP6f signal in individual cardiomyocytes to be extracted, providing quantification of calcium transients from single cells throughout the heartbeat (Fig. 8b). As an example of a vascular measurement from the same stack, we measured changes in the width of a nearby vessel as a function of the cardiac cycle, and found width decreased to 83% (22.7 μm decrease) of its maximum diameter at ~75% of the cardiac cycle (Fig 8c). Irradiation with high laser power can induce a sterile lesion that alters calcium handling(Davalos et al., 2005). In a different region in the same heart, higher power laser irradiation resulted in increased GCaMP6f fluorescence intensity compared to surrounding cells. Below the lesion, a subset of cardiomyocytes (cells 4-6 in Fig. 8d) displayed aberrant calcium dynamics that were not synchronized with the surrounding region (cells 1-3 in Fig. 8d).

3.3.3 Cardiac- and respiratory-cycle decoupling enables quantification of depth-dependent calcium dynamics

To highlight the effects of breathing and heartbeat, GCaMP6f and vascular Texas Red fluorescence, normalized by the maximum intensity at each depth, from one imaged volume is displayed as a 2D function of both the cardiac and respiratory cycle (Fig. 9). The GCaMP6f signal exhibited a cardiac-cycle dependent peak consistent with measurements in ex vivo preparations (Rubart et al., 2003b) (Fig. 9a and c), as well as a respiratory-cycle dependent decrease near the peak lung pressure (Fig. 9a and d). In this stack, signal from the vascular label decreased shortly after the R-wave and exhibited a respiration-dependent decrease that mirrored that of the GCaMP6f signal (Fig. 9b, e and f). However, averaged over multiple stacks, Texas Red fluorescence remained constant across the cardiac cycles and nearly constant across respiratory cycles, while GCaMP6f had both cardiac and, to a lesser extent, respiratory cycle variation (Fig. 10, eight stacks in three animals). In wild type mice that did not express the calcium indicator, we imaged autofluorescence using the same emission filters used for GCaMP6f and observed a small increase in intensity within the first half of cardiac cycle (Fig. 16a). The raw change in the fluorescence intensity, however, was about 90 times smaller than in GCaMP6f-expressing mice. To study the effect of depth, we measured the GCaMP6f and vascular label signals across both the respiratory cycle and cardiac cycle as a function of position below the heart surface (Fig. 10g and h). We calculated rise time and decay time (Hammer et al., 2014) of the GCaMP6f signal across the cardiac cycle as a function of imaging depth (eight stacks from three mice, data from 25-50% of the respiratory cycle excluded to avoid confounding effects of the respiratory-dependent fluorescent intensity fluctuation) and found that both rise and decay times remained relatively constant over depths from 15 to 90 μm ($p = 0.67$, $p = 0.97$, ANOVA) with mean values of 32 ± 7 and 103 ± 34 ms,

respectively, and are consistent with other measurements with GCaMP6f (Hammer et al., 2014) (Fig. 10c and d).

3.3.4 Displacement in the myocardium is dependent on the cardiac and respiratory cycles

Tissue displacement relative to the stabilized probe was dependent on both heart contraction and lung inflation. To quantify this motion throughout the cardiac cycle, point-like structures, such as the edge of a capillary bifurcation, were manually tracked in 3D in reconstructed stacks (Fig. 11a; binned by 5% of the cardiac cycle, averaged over the second half of respiratory cycle). In-plane displacements (base-apex (x) and anterior-posterior (y)) from the initial positions at the start of the cardiac cycle had an elliptical profile and were larger (32.4 ± 31.6 μm, mean ± standard deviation, and 32.3 ± 31.3 μm, respectively; 14 measurements across three animals) than out of plane in the axial (depth in myocardium) direction (3.9 ± 4.7 μm) (Fig. 11b and d), During the respiratory cycle, displacements from the position at lowest ventilation pressure in the base-apex and anterior to posterior directions were small, while structures moved in the ventral, out-of-plane direction by 9.5 μm ± 3.8 around the time of peak lung inflation (Fig. 11c and e; averaged over second half of cardiac cycle, 5% binning along respiratory cycle).

3.4 Discussion

Multiphoton microscopy of GCaMP6f-expressing mice provides a novel method to study in vivo excitation-contraction coupling. Using the combination of fast image acquisition, surgical stabilization, image reconstruction algorithms, and a genetically encoded calcium reporter, we demonstrated the ability to image and quantify in vivo calcium transients at single-cell resolution in the beating mouse heart during respiration. This enabled the measurement of aberrant calcium activity in individual cells within the tissue. Furthermore, this technique allows the simultaneous

quantification of additional in vivo cardiac dynamics including displacement and vessel width changes at each phase of the cardiac and respiratory cycles. Figure 6 summarizes the relative timing of physiologic dynamics over the cardiac and respiratory cycles. Data aggregated across three animals show that the GCaMP6f fluorescence peak precedes the maximum in-plane displacement but coincides with the out-of-plane motion in cardiac cycle. Such measurements enable novel assays of the relationship between excitation and mechanical output.

Figure 12 summarizes the relative timing of physiologic dynamics over the cardiac and respiratory cycles. Data aggregated and normalized across three animals show that the GCaMP6f fluorescence peak proceeds the ventricular R-wave, and is then followed by base-apex and anterior-posterior motion occurring within the image plane, resulting in the dominant component of cardiac motion. This temporal relationship between cardiomyocyte excitation-contraction coupling, and the role of calcium, has been widely demonstrated in vitro and ex vivo perfused heart, yet has not been demonstrated in the true in vivo environment. Out-of-plane motion in the cardiac cycle coincides with GCaMP6f peak fluorescence, however is minimal and within the standard deviation of change (Fig 10b), likely demonstrating an insignificant occurrence to the temporal relationship of excitation-contraction coupling. Cardiac dependent Texas-Red vascular fluorescence shows high frequency fluctuations when averaged across shallow axial sections, as shown in Fig. 9h and Fig. 16h, and likely attributed to aggregate fluorescence on capillaries that is modulating in and out of plane at sub axial sampling scale, as these intensity variations are not present in regions containing only vasculature (data not shown). These fluctuations do average out when looking at whole stack or across animal data since they approximately randomly distributed. The cardiac dependent variation seen in Fig. 12 can be attributed to noise that is enhanced by normalizing the signal to compare objectively

across data types. These measurements enable novel assays of the relationship between excitation and mechanical output. We also note that GCaMP6f has a $t_{1/2\,(off)}$ time of 288 ms, meaning that our measured decay is overestimated (Helassa, Podor, Fine, & Torok, 2016).

Multiple aspects of these measurements suggest that variation of GCaMP6f intensity across the cardiac cycle is largely attributable to changes in calcium concentration. The contribution of autofluorescence (Fig. 16), which is likely dominated by NADH (Zipfel et al., 2003; Blinova et al., 2004), was small compared to the GCaMP6f signal. The volume of cardiomyocytes stays approximately constant throughout contraction (Sonnenblick et al., 1967; Rodriguez et al., 1992; Leu et al., 2001), so that the concentration of GCaMP6f likely stays the same and does not contribute to the signal change. The fluorescence from the vascular label stayed constant over the cardiac cycle, although individual planes showed fluctuations both increasing and decreasing which tended to match timing of the out-of-plane motion, peaking around 25% of the cardiac cycle (for example, Fig. 9h). The lack of cardiac-cycle dependence of the vascular channel suggests that optical or motion effects, which would be similar in both fluorescence channels, likely do not account for the change in the GCaMP6f cardiac-dependent signal. Relative to the respiratory cycle, the GCaMP6f and vascular signals had a minimum around 35% of the respiratory cycle which also coincided with the timing of the maximum out-of-plane displacement and ventilator pressure (Fig. 12b). While we cannot completely rule out a contribution from out-of-plane motion effects on the GCaMP6f intensity increase during the cardiac cycle, we can argue that the magnitude of the effect of cardiac cycle motion must be less than that of breathing motion because the breathing displacement is larger than the cardiac cycle displacement. This suggests that motion, at worst, can only account for a small fraction of the cardiac cycle GCaMP6f signal intensity change.

Both breathing and heartbeat change the shape and composition of tissue so that future studies will need to take the resulting changes in path length, absorption, scattering, and wavefront distortion into account.

Our methods enable simultaneous measurement and visualization of multiple aspects of cardiac physiology at the cellular scale, including motion, calcium activity, and vasculature. The time resolution of the acquisition allows data collection throughout systolic contraction of the cardiomyocyte. Allowing the animal to respire during measurements enables studies of the coupling between respiratory and cardiac function and facilitates studies of disease models that could be confounded by breath holds. Although both clinical practice and experimental protocols take advantage of the coupling between breathing and cardiac function, an understanding of the relationship between the respiration and cardiac function, such as the diving reflex in which a breath hold decreases heart rate (Panneton, 2013), is still incomplete. Breathing also exerts forces on the cardiac tissue which could influence tissue perfusion and cardiomyocyte function in both disease and healthy individuals.

In this method, there is a tradeoff between 1. the degree of binning in cardiac and respiratory phase and in the extent of spatial averaging and 2. the amount of time spent imaging to acquire sufficient data at a given depth. We demonstrated that 1.5-3s of image acquisition per axial plane is sufficient for characterization across both respiratory and cardiac cycles, so experiments involving stacks before and after a manipulation or time-lapse studies are quite feasible. Methodological limitations include the direct adherence of the window to the cardiac tissue, which, although the region of adhesive is limited as much as possible with to a thin ring, could alter tissue function. This preparation does allow recovery procedures in which the probe is removed and the animal recovers, but repeated open chest surgeries are a practical limitation.

While faster imaging modalities such as ultrasound (Cikes et al., 2010) and OCT (Srinivasan et al., 2010) can measure tissue motion and blood flow more conveniently that MPM, fluorescence techniques have the advantage of the availability of many functional indicators such as GCaMP6f and label specificity through promoter-driven reporter gene expression. Combined with our protocol for in vivo imaging, this makes multiphoton microscopy a potent tool for cardiac studies.

REFERENCES

Aguirre, A.D., Vinegoni, C., Sebas, M., and Weissleder, R. (2014). Intravital imaging of cardiac function at the single-cell level. Proc Natl Acad Sci U S A 111(31), 11257-11262. doi: 10.1073/pnas.1401316111.

Blinova, K., Combs, C., Kellman, P., and Balaban, R.S. (2004). Fluctuation analysis of mitochondrial NADH fluorescence signals in confocal and two-photon microscopy images of living cardiac myocytes. J Microsc 213(Pt 1), 70-75.

Cerami, L., Mazur, E., Nolte, S., and Schaffer, C.B. (2013). "Femtosecond Laser Micromachining," in Ultrafast Nonlinear Optics, eds. R. Thomson, C. Leburn & D. Reid. (Heidelberg: Springer), 287-321.

Chen, T.W., Wardill, T.J., Sun, Y., Pulver, S.R., Renninger, S.L., Baohan, A., et al. (2013). Ultrasensitive fluorescent proteins for imaging neuronal activity. Nature 499(7458), 295-300. doi: 10.1038/nature12354.

Cianchetti, F.A., Kim, D.H., Dimiduk, S., Nishimura, N., and Schaffer, C.B. (2013). Stimulus-evoked calcium transients in somatosensory cortex are temporarily inhibited by a nearby microhemorrhage. PLoS One 8(5), e65663. doi: 10.1371/journal.pone.0065663.

Cikes, M., Sutherland, G.R., Anderson, L.J., and Bijnens, B.H. (2010). The role of echocardiographic deformation imaging in hypertrophic myopathies. Nat Rev Cardiol 7(7), 384-396. doi: 10.1038/nrcardio.2010.56.

Davalos, D., Grutzendler, J., Yang, G., Kim, J.V., Zuo, Y., Jung, S., et al. (2005). ATP mediates rapid microglial response to local brain injury in vivo. Nat Neurosci 8(6), 752-758. doi: 10.1038/nn1472.

Fujiwara, K., Tanaka, H., Mani, H., Nakagami, T., and Takamatsu, T. (2008). Burst emergence of intracellular Ca2+ waves evokes arrhythmogenic oscillatory

depolarization via the Na+-Ca2+ exchanger: simultaneous confocal recording of membrane potential and intracellular Ca2+ in the heart. Circ Res 103(5), 509-518. doi: 10.1161/CIRCRESAHA.108.176677.

Ghouri, I.A., Kelly, A., Burton, F.L., Smith, G.L., and Kemi, O.J. (2015). 2-Photon excitation fluorescence microscopy enables deeper high-resolution imaging of voltage and Ca(2+) in intact mice, rat, and rabbit hearts. J Biophotonics 8(1-2), 112-123. doi: 10.1002/jbio.201300109.

Hammer, K.P., Hohendanner, F., Blatter, L.A., Pieske, B.M., and Heinzel, F.R. (2014). Variations in local calcium signaling in adjacent cardiac myocytes of the intact mouse heart detected with two-dimensional confocal microscopy. Front Physiol 5, 517. doi: 10.3389/fphys.2014.00517.

Hayashi, S., and McMahon, A.P. (2002). Efficient recombination in diverse tissues by a tamoxifen-inducible form of Cre: a tool for temporally regulated gene activation/inactivation in the mouse. Dev Biol 244(2), 305-318. doi: 10.1006/dbio.2002.0597.

Helassa, N., Podor, B., Fine, A., & Torok, K. (2016). Design and mechanistic insight into ultrafast calcium indicators for monitoring intracellular calcium dynamics. *Sci Rep, 6*, 38276. doi:10.1038/srep38276

Jaimes, R., 3rd, Walton, R.D., Pasdois, P., Bernus, O., Efimov, I.R., and Kay, M.W. (2016). A technical review of optical mapping of intracellular calcium within myocardial tissue. Am J Physiol Heart Circ Physiol 310(11), H1388-1401. doi: 10.1152/ajpheart.00665.2015.

Jung, K., Kim, P., Leuschner, F., Gorbatov, R., Kim, J.K., Ueno, T., et al. (2013). Endoscopic time-lapse imaging of immune cells in infarcted mouse hearts. Circ Res 112(6), 891-899. doi: 10.1161/CIRCRESAHA.111.300484.

Kleinfeld, D., Mitra, P.P., Helmchen, F., and Denk, W. (1998). Fluctuations and stimulus-induced changes in blood flow observed in individual capillaries in layers 2 through 4 of rat neocortex. Proceedings of the National Academy of Sciences USA 95, 15741-15746.

Kuzmiak-Glancy, S., Jaimes, R., 3rd, Wengrowski, A.M., and Kay, M.W. (2015). Oxygen demand of perfused heart preparations: how electromechanical function and inadequate oxygenation affect physiology and optical measurements. Exp Physiol 100(6), 603-616. doi: 10.1113/EP085042.

Lee, S., Vinegoni, C., Feruglio, P.F., Fexon, L., Gorbatov, R., Pivoravov, M., et al. (2012). Real-time in vivo imaging of the beating mouse heart at microscopic resolution. Nat Commun 3, 1054. doi: 10.1038/ncomms2060.

Leu, M., Ehler, E., and Perriard, J.C. (2001). Characterisation of postnatal growth of the murine heart. Anat Embryol (Berl) 204(3), 217-224.

Li, W., Nava, R.G., Bribriesco, A.C., Zinselmeyer, B.H., Spahn, J.H., Gelman, A.E., et al. (2012). Intravital 2-photon imaging of leukocyte trafficking in beating heart. J Clin Invest 122(7), 2499-2508. doi: 10.1172/JCI62970.

Mortality, G.B.D., and Causes of Death, C. (2015). Global, regional, and national age-sex specific all-cause and cause-specific mortality for 240 causes of death, 1990-2013: a systematic analysis for the Global Burden of Disease Study 2013. Lancet 385(9963), 117-171. doi: 10.1016/S0140-6736(14)61682-2.

Mozaffarian, D., Benjamin, E.J., Go, A.S., Arnett, D.K., Blaha, M.J., Cushman, M., et al. (2015). Heart disease and stroke statistics--2015 update: a report from the American Heart Association. Circulation 131(4), e29-322. doi: 10.1161/CIR.0000000000000152.

Panneton, W.M. (2013). The mammalian diving response: an enigmatic reflex to preserve life? Physiology (Bethesda) 28(5), 284-297. doi: 10.1152/physiol.00020.2013.

Pologruto, T.A., Sabatini, B.L., and Svoboda, K. (2003). ScanImage: flexible software for operating laser scanning microscopes. Biomed Eng Online 2, 13. doi: 10.1186/1475-925X-2-13.

Pologruto, T.A., Yasuda, R., and Svoboda, K. (2004). Monitoring neural activity and [Ca2+] with genetically encoded Ca2+ indicators. J Neurosci 24(43), 9572-9579. doi: 10.1523/JNEUROSCI.2854-04.2004.

Prevedel, R., Verhoef, A.J., Pernia-Andrade, A.J., Weisenburger, S., Huang, B.S., Nobauer, T., et al. (2016). Fast volumetric calcium imaging across multiple cortical layers using sculpted light. Nat Methods 13(12), 1021-1028. doi: 10.1038/nmeth.4040.

Pries, A.R., and Reglin, B. (2017). Coronary microcirculatory pathophysiology: can we afford it to remain a black box? Eur Heart J 38(7), 478-488. doi: 10.1093/eurheartj/ehv760.

Rodriguez, E.K., Hunter, W.C., Royce, M.J., Leppo, M.K., Douglas, A.S., and Weisman, H.F. (1992). A method to reconstruct myocardial sarcomere lengths and orientations at transmural sites in beating canine hearts. Am J Physiol 263(1 Pt 2), H293-306. doi: 10.1152/ajpheart.1992.263.1.H293.

Rubart, M., Pasumarthi, K.B., Nakajima, H., Soonpaa, M.H., Nakajima, H.O., and Field, L.J. (2003a). Physiological coupling of donor and host cardiomyocytes after cellular transplantation. Circ Res 92(11), 1217-1224. doi: 10.1161/01.RES.0000075089.39335.8C.

Rubart, M., Soonpaa, M.H., Nakajima, H., and Field, L.J. (2004). Spontaneous and evoked intracellular calcium transients in donor-derived myocytes following

intracardiac myoblast transplantation. J Clin Invest 114(6), 775-783. doi: 10.1172/JCI21589.

Rubart, M., Wang, E., Dunn, K.W., and Field, L.J. (2003b). Two-photon molecular excitation imaging of Ca2+ transients in Langendorff-perfused mouse hearts. Am J Physiol Cell Physiol 284(6), C1654-1668. doi: 10.1152/ajpcell.00469.2002.

Santisakultarm, T.P., Cornelius, N.R., Nishimura, N., Schafer, A.I., Silver, R.T., Doerschuk, P.C., et al. (2012). In vivo two-photon excited fluorescence microscopy reveals cardiac- and respiration-dependent pulsatile blood flow in cortical blood vessels in mice. Am J Physiol Heart Circ Physiol 302(7), H1367-1377. doi: 10.1152/ajpheart.00417.2011.

Scherschel, J.A., Soonpaa, M.H., Srour, E.F., Field, L.J., and Rubart, M. (2008). Adult bone marrow-derived cells do not acquire functional attributes of cardiomyocytes when transplanted into peri-infarct myocardium. Mol Ther 16(6), 1129-1137. doi: 10.1038/mt.2008.64.

Shih, A.Y., Driscoll, J.D., Drew, P.J., Nishimura, N., Schaffer, C.B., and Kleinfeld, D. (2012). Two-photon microscopy as a tool to study blood flow and neurovascular coupling in the rodent brain. J Cereb Blood Flow Metab 32(7), 1277-1309. doi: 10.1038/jcbfm.2011.196.

Smart, N., Bollini, S., Dube, K.N., Vieira, J.M., Zhou, B., Davidson, S., et al. (2011). De novo cardiomyocytes from within the activated adult heart after injury. Nature 474(7353), 640-644. doi: 10.1038/nature10188.

Sonnenblick, E.H., Ross, J., Jr., Covell, J.W., Spotnitz, H.M., and Spiro, D. (1967). The ultrastructure of the heart in systole and diastole. Chantes in sarcomere length. Circ Res 21(4), 423-431.

Srinivasan, V.J., Sakadzic, S., Gorczynska, I., Ruvinskaya, S., Wu, W., Fujimoto, J.G., et al. (2010). Quantitative cerebral blood flow with optical coherence tomography. Opt Express 18(3), 2477-2494. doi: 10.1364/OE.18.002477.

Tallini, Y.N., Ohkura, M., Choi, B.R., Ji, G., Imoto, K., Doran, R., et al. (2006). Imaging cellular signals in the heart in vivo: Cardiac expression of the high-signal Ca2+ indicator GCaMP2. Proc Natl Acad Sci U S A 103(12), 4753-4758. doi: 10.1073/pnas.0509378103.

Tao, W., Shi, J., Dorn, G.W., 2nd, Wei, L., and Rubart, M. (2012). Spatial variability in T-tubule and electrical remodeling of left ventricular epicardium in mouse hearts with transgenic Galphaq overexpression-induced pathological hypertrophy. J Mol Cell Cardiol 53(3), 409-419. doi: 10.1016/j.yjmcc.2012.06.006.

Vinegoni, C., Aguirre, A.D., Lee, S., and Weissleder, R. (2015a). Imaging the beating heart in the mouse using intravital microscopy techniques. Nat Protoc 10(11), 1802-1819. doi: 10.1038/nprot.2015.119.

Vinegoni, C., Lee, S., Aguirre, A.D., and Weissleder, R. (2015b). New techniques for motion-artifact-free in vivo cardiac microscopy. Front Physiol 6, 147. doi: 10.3389/fphys.2015.00147.

Wasserstrom, J.A., Shiferaw, Y., Chen, W., Ramakrishna, S., Patel, H., Kelly, J.E., et al. (2010). Variability in timing of spontaneous calcium release in the intact rat heart is determined by the time course of sarcoplasmic reticulum calcium load. Circ Res 107(9), 1117-1126. doi: 10.1161/CIRCRESAHA.110.229294.

Zipfel, W.R., Williams, R.M., Christie, R., Nikitin, A.Y., Hyman, B.T., and Webb, W.W. (2003). Live tissue intrinsic emission microscopy using multiphoton-excited native fluorescence and second harmonic generation. Proc Natl Acad Sci U S A 100(12), 7075-7080. doi: 10.1073/pnas.0832308100.

CHAPTER 4

OPTICAL PARAMETERS FOR IN VIVO MULTIPHOTON MICROSCOPY OF BEATING MOUSE HEART

4.1 Introduction

Despite pharmacological advances improving our ability to slow progression of heart disease, the creation of more effective stent technology, and advancement in the maintenance of arrhythmogenic tissue following infarction, heart disease remains the leading cause of death globally. Conditions such as microvascular angina and heart failure with preserved ejection fraction persist in a large percentage of patients and treatment strategies remain unclear (Pries & Reglin, 2017). Additionally, therapeutic approaches using viral reprogramming and engineered tissue, which have been successful in animal models have failed to reach the clinic, indicating that technologies used in animal studies are failing to recapitulate conditions present in the in vivo microenvironment. In the last decade, the field of neuroscience has realized the benefits of multiphoton microscopy alongside advances in genetic tools allowing precise quantitative study of the activity of individual neurons within large cell populations in vivo, bridging major gaps in our understanding of circuit level brain activity. Recently, NOPA's functioning in the 1300-1700 nm range have become commercially available. These laser sources enable optical imaging using three-photon excitation (3PE) microscopy into areas of the brain not previously reachable. We (Jones, Small, & Nishimura, 2018), and others, (Aguirre, Vinegoni, Sebas, & Weissleder, 2014; Hatzistergos et al., 2016; Lee et al., 2012; Li et al., 2012) have recently demonstrated two-photon excitation (2PE) microscopy of the beating heart in mice. Increased imaging depth would allow study of disease mechanisms involved in

deeper structures such as the penetrating branches of coronary artery architecture, which morphologically vary as a function of depth into the endocardium.

The utility of 3PE microscopy depends on tissue properties and application-related constraints that are unique to the heart that need to be measured and optimized. To our knowledge there have been no studies investigating the performance and utility of such information in beating cardiac tissue in vivo. Here, we measure optical parameters critical to optimizing multipthoton microscopy in the near infrared (NIR) wavelength in beating heart as a first step toward the application of these technologies to study the heart.

For a given wavelength, the characteristic attenuation length (CAL), defined as $l_e = \left(\frac{1}{l_a} + \frac{1}{l_s}\right)^{-1}$ where l_a is the absorption length and l_s is the scattering length, sets the physical limitation of the imaging depth achievable in a tissue. Due to the highly scattering nature of cardiac tissue, the achievable depth of imaging with multiphoton microscopy is limited and stands to benefit from excitation sources further into the NIR where there are regions with less attenuation from water. The higher contrast achieved using 3PE also would be beneficial to quantify high-resolution structures such as sarcomeres of the cardiomyocytes. The increase in signal gained from higher repetition rate laser sources is limited by the thermal capacity of the tissue. In order to record images unaffected by systolic contractile motion, which is required to study cardiac dynamics, scanning must be performed at a high speed, requiring higher repetition rate lasers to provide sufficient pulses per pixel. The cardiac muscle is drastically different from brain and the capacity to dissipate high-powered laser energy in vivo has not been explored.

Here, we measure the characteristic attenuation length of heart tissue in vivo and explore the utility of femtosecond excitation sources throughout the range of wavelengths reported for multiphoton microscopy using both 2PE and 3PE driven processes. Due to the abundance of large vessels relative to the FOV in the ventricle, we investigate the properties of capillary-rich myocardial tissue and the larger post-capillary venules separately. We use a custom, high frame rate, multiphoton imaging system, equipped with a NOPA, capable of tuning to 1700 nm for 3PE, as well as a Ti:Sapphire laser (Chameleon) for 2PE, to characterize the effect of scattering throughout the broad range of wavelengths.

4.2 Methods

4.2.1 Animal surgical procedure

Mice were anesthetized with ketamine (10 mg/mL) and xylazine (1 mg/mL) in saline via intraperitoneal injection (0.1 mL/10g body weight) and then intubated via the trachea using a 22-gauge, 1-inch catheter to allow mechanical ventilation (95 breath/min, 12 cm H_2O end-inspiratory pressure; CWE Inc. SAR-830/P ventilator) with medical grade oxygen and 1.5% isoflurane for maintaining anesthesia. The ventilation rate was selected for optimum animal stability and also to avoid harmonics of the heart rate so that the cardiac and respiratory cycles were out of phase. The mouse was positioned on its right side, on top of a motorized stage with a heating pad to maintain body temperature at 37.5 ºC. Hair over the left thorax was depilated, skin and muscle layers over the chest wall excised, and the intercostal space between ribs 7 and 8 perforated and retracted to create space for placement of the window. Following removal of the pericardial sac, a stabilization probe was attached to the left ventricle free-wall using tissue adhesive as described previously (Jones et al., 2018). ECG electrodes were attached to 21 gauge needles inserted subcutaneously through the

front and contralateral hind limb, connected through an isolated differential amplifier (World Precision Instruments; #ISO-80), and recorded inside a Faraday enclosure mounted to the microscope. ECG and ventilation pressure (from ventilator) signals were continuously monitored on an oscilloscope and recorded simultaneously with image acquisition. 5% glucose in saline (0.1 mL/10 g body weight) and 0.15 mg/mL atropine sulfate (5 µg/100 g body weight) were injected subcutaneously every 30 min throughout surgery and in vivo microscopy. This procedure allowed stable in vivo imaging for 3 h. A retro-orbital injection of Texas-Red conjugated, 70 kDa, neutral dextran (3% in saline; Thermo #D1830), and fluorescein conjugated dextran, 70 kDa , anionic (3% Thermo #D1823) was performed to label blood plasma providing contrast in the vasculature. For cryoinfarction imaging, a thoracotomy was performed allowing a liquid-nitrogen-cooled probe with a 3 mm diameter to be touched to the surface of the left ventricle for 8 – 10 sec twice. 6-0 silk sutures were used to close the rib, muscle and skin layers, allowing the mouse to regain natural respiration. Following 7-days of recovery, the same surgical procedure was performed for in vivo cardiac imaging. To compensate for the reduced density of fluorophores due to a loss of cardiomyocytes and vasculature within the infarcted tissue, homozygous $Cx3Cr1^{GFP/GFP}$ mice (B6.129P-Cx3cr1tm1Litt/J; Jax stock No: 005582) (Jung, 2000) were bred to homozygous $CCR2^{RFP/RFP}$ mice (B6.129(Cg)-Ccr2tm2.1Ifc/J; Jax stock No: 017586) (Saederup et al., 2010) to generate double transgenic hemizygous $Cx3Cr1^{-/GFP}$-$Ccr2^{-/RFP}$ mice, and were used for in vivo imaging of cryoinfarcted myocardium since fluorescence is generated from monocyte populations common to injured myocardium.

4.2.2 Microscopy and laser source

Imaging was conducted using a custom multiphoton microscope with two detection channels and an 8-kHz resonant scanner (Cambridge Technology) imaged onto a galvanometric (galvo) pair (Cambridge Technology) to allow for both high frame rate imaging with resonant scanning and arbitrary pattern scanning with galvo scanning. Resonant scanning data acquisition was performed using a National Instruments digitizer (NI-5734), FPGA (PXIe-7975), and multifunction I/O module (PXIe-6366) for device control, mounted in a PXI chassis (PXIe-1073) controlled by ScanImage 2016b (Pologruto, Sabatini, & Svoboda, 2003). 1300 nm and 1700 nm laser light was generated by a NOPA (Coherent, Opera-F) pumped by a diode-pumped, amplified femtosecond laser (60 μJ/pulse at 1 MHz; Coherent, Monaco). Dispersion for 1,300-nm excitation was compensated with an SF11 prism pair (Ouzounov et al., 2017). For 1,700-nm lasers, dispersion is compensated using stacked silicon wafers (University Wafer ID# 2808) set at Brewster's angle (Horton & Xu, 2015). A Ti:Sapph laser (Chameleon, Coherent) was used for 2PE imaging at 900 nm or 775 nm. Imaging was performed from 1-30 fps as noted. Images were acquired with two Olympus XLPlan N 25x 1.05 NA objectives, one optimized for high transmission of 1700 nm light. Emission was separated using wavelength specific primary dichroic (Semrock FF705-Di01-49x70, BLP01-980R-49x70), a secondary dichroic (Semrock FF593-Di03-90x108), and bandpass filters selective for fluorescein (517/65) and Texas-red (629/56). Each sequential stack within an ROI was started at the halfway point of the previous stack, and power was adjusted so that the top of the stack was not saturated and the bottom of the stack still had signal. As stacks moved deeper, the total depth of the stack was decreased since signal was lost quicker due to the exponential attenuation of the excitation light.

4.2.3 Calculation of characteristic attenuation length.

To investigate the cardiorespiratory impact on the tissue optical properties we separately quantified the characteristic attenuation length within a large vessel (diameter $\geq 50\,\mu m$) and within surrounding myocardium in areas lacking large vessels. For each axial slice, a time lapse of 50 images was taken, which has been shown previously to generate sufficient data to populate all cardiorespiratory phases (Jones et al., 2018). The cardiac and respiratory cycles were normalized per each breath/beat so that the position in each unique cycle was expressed as a percentage of that cycle. Fluorescent intensity of pixels in the top 0.1% of values within a frame that fell in a 5% x 5% window of the cardiac and respiratory cycles respectively, were averaged. Each data point in the signal decay curve represents the average of all pixels within one frame that occurred during the given phase of the cardiorespiratory cycle. If there is no data satisfying the gating criteria for a given frame then no data point is generated for that frame. The number of pixels averaged from a frame varies with heart rate and the peak respiratory pressure being driven by the ventilator. Due to this variation, some frames contain no data from a given phase. A linear curve was fit to the log plot of the signal decay. For power adjustments occurring between consecutive stacks, the intensity of the background due to the electronic noise floor was subtracted and the signal intensity adjusted according to

$$< F(t)_{2p} > \propto < P >^2 \, e^{\frac{-2z}{l_e}}$$

for 2PE and

$$< F(t)_{3p} > \propto < P >^3 \, e^{\frac{-3z}{l_e}}$$

for 3PE. Where $< P >$ is the time averaged power, z is the imaging depth in the tissue, and l_e is the characteristic attenuation length (Horton et al., 2013). Stacks were started well above the tissue surface so that a clear rise in fluorescent signal was apparent at the start of the stack showing the boundary of the tissue surface. Regions

were defined as either microvasculature or capillary-rich myocardial tissue based on averaged projections of the 50 frame image series at each z slice that show the average location of the microvessels over the entire trajectory of tissue motion (Fig. 2). Continuous regions that only contained vessels $< 50\ \mu m$ in diameter were categorized as myocardium.

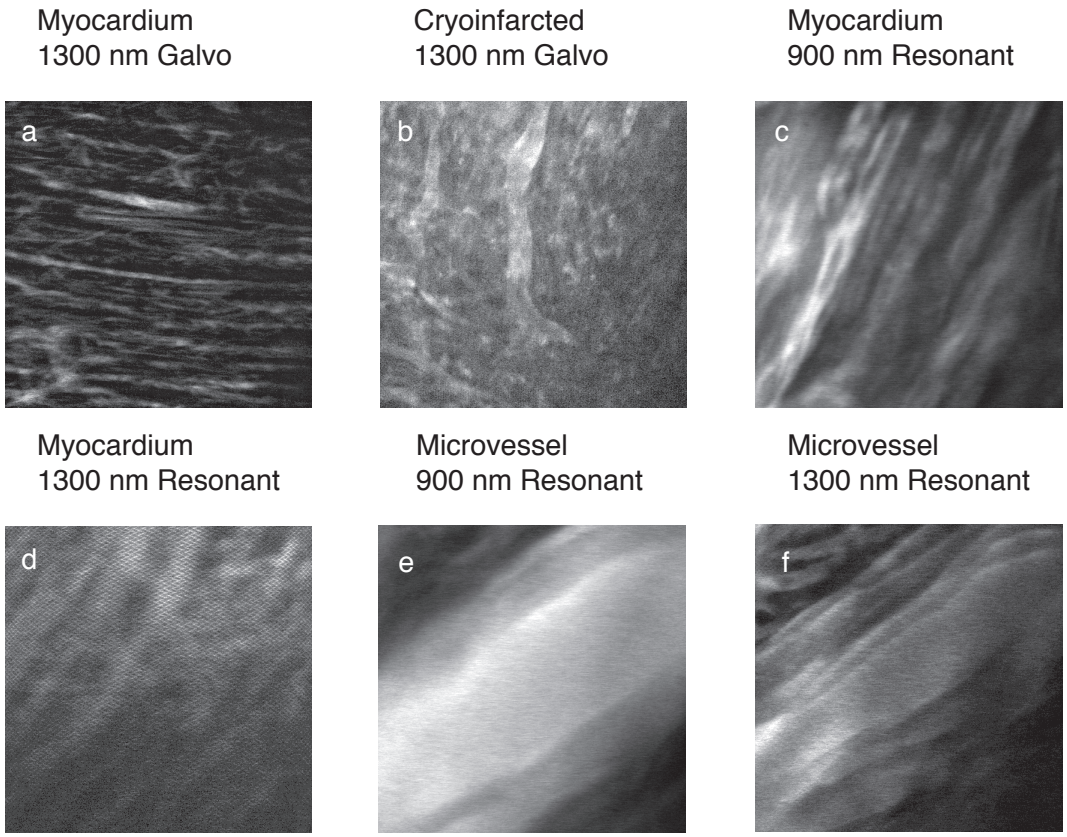

Figure 17. Average intensity projections of one z slice within cardiac tissue showing examples of the morphological features analyzed in Figure 18. a) Healthy myocardium with galvanometric (galvo) scanning using 1300 nm 3PE. b) Cryoinfarcted myocardium with galvo using 1300 nm 3PE. c) Healthy myocardium with resonant scanning using 900 nm 2PE. d) Healthy myocardium with resonant scanning using 1300 nm 3PE. e) Healthy microvesssel with resonant scanning using 900 nm 2PE. f) Healthy microvessel with resonant scanning 3PE.

4.3 Results

We measured the intensity of 2PE and 3PE fluorescence from dyes in vasculature excited by several different wavelengths in image stacks taken at constant power with example images shown in Fig. 17. Fig. 18a shows the fluorescent intensity as function of depth normalized to $< P >^2$ or $< P >^3$ in a single animal (Kobat et al., 2009). Discontinuities in the plots of ln(signal) versus depth were observed throughout the stacks (Fig. 18a). Within the left ventricle of a mouse, the upper few hundred micrometers of tissue is densely populated with large microvasculature, making it likely to encounter a region which is obstructed by large vessels when the field of view is 250 μm across and more than 100 μm deep. Therefore, we report CAL measurements through a large (> 50 μm) surface vessel separately (labeled microvessel). In the regions labeled as myocardium the capillaries are distributed throughout the tissue and were used as the source of the fluorescent signal for this measurement. The myocardium without large vessels consistently has a longer CAL than the large blood vessels across all excitations wavelengths.

To investigate the impact of the motion of the beating heart, compression of the vasculature, and axial motion resulting from the respiring lungs, we analyzed CAL as a function of the cardiac and respiratory cycle. The curves of log signal versus depth regained a linear trend in the myocardium when the data were restricted to 5% of cardiac and 5% of respiratory cycles (Fig. 19). In all cases, measurements that were restricted by cardiorespiratory phase resulted in an increased estimate of CAL relative to the aggregated estimate as shown in Fig. 18b. For both 1300 and 900 nm excitation, there does not appear to be a strong dependence on either cardiac or respiratory cycle (Fig. 20). In the beating heart, we found the averaged cardiorespiratory-phase-aligned CAL in the myocardium to be 97 μm for 900-nm, 2PE excitation, 160 μm for 1300-nm, 3PE excitation, and 204 μm for 1700-nm, 3PE

excitation. For cryoinfarcted tissue, we found that the CAL to be 106 μm for 900-nm excitation and 161 μm for 1300-nm excitation.

Ultimately, thermal damage is the limiting factor when increasing the average power of a source used for imaging. In a preliminary study of thermally dissipative capacity of myocardial tissue using resonant scanning, the 1300 nm light was focused through a large microvessel at a depth of 250 μm below the tissue surface for ~ 1 minute at 300 mW. We found there was no drop in fluorescence signal due to a change in scattering due to surface damage. A lower intensity stack taken after scanning at full power at depth revealed there was no broadband autofluorescence emission normally associated with high power tissue damage. This indicates that the heart may be able to withstand more thermal energy in vivo than brain.

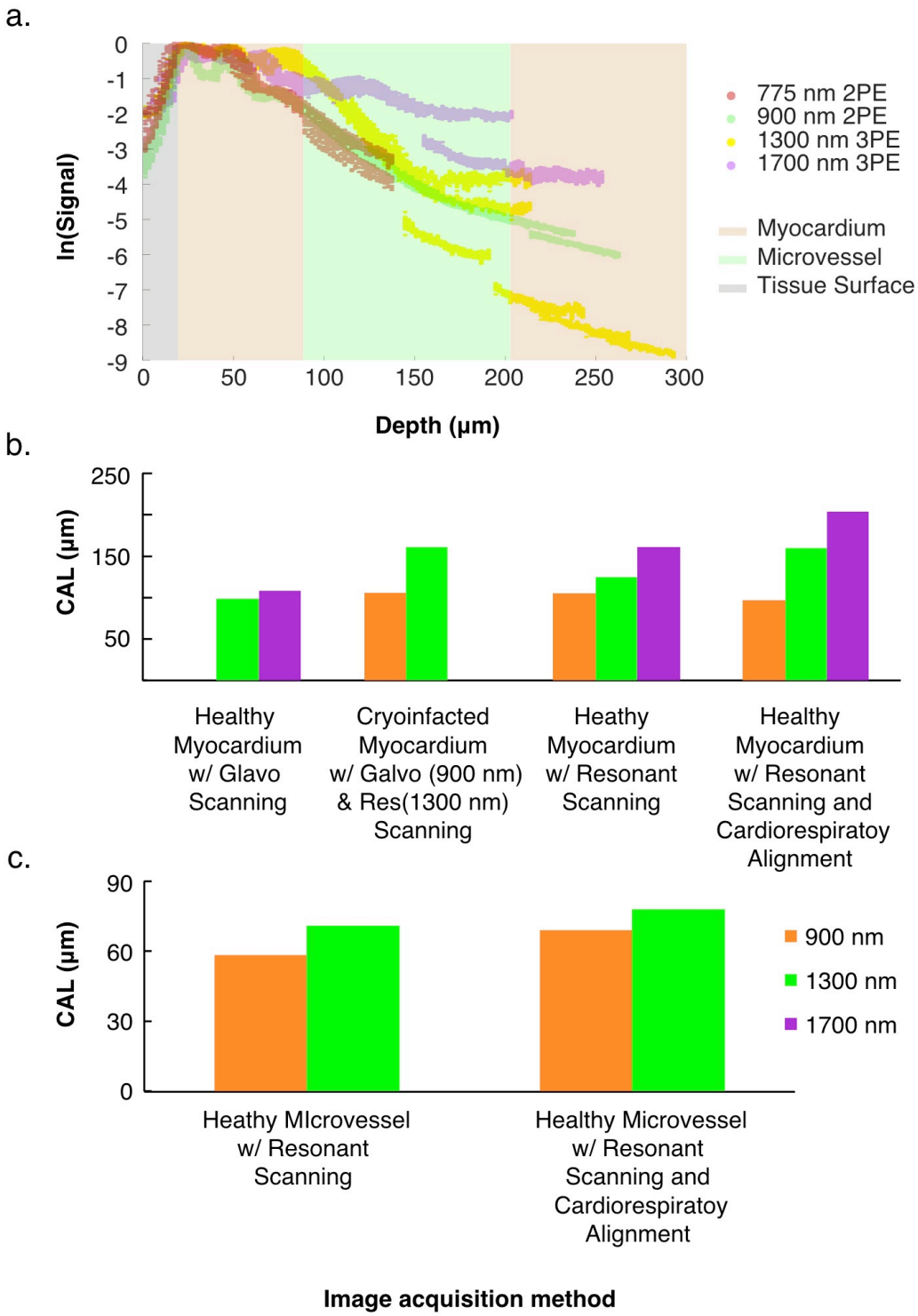

Figure 18. Comparison of CAL in ventricle using two- and three- photon excitation with various wavelengths. a. Fluorescent signal through large vessel in same animal driven by two- and three-photon processes in the beating heart averaged

over the cardiorespiratory cycle. Data shows top 0.1% of signal in stacks taken through a large vessel with varying wavelengths and represents 3-8 stacks taken in 2 μm steps axially with a power adjustment at each stack. Two and three photon signal data were normalized for incident power. b. Impact of high-speed imaging and cardiorespiratory alignment on CAL quantification in healthy and diseased myocardial tissue through NIR. c. CAL in large microvessel measured with 1300 nm using 3PE and 900 nm using 2PE-driven processes showing impact of cardiorespiratory phase alignment.

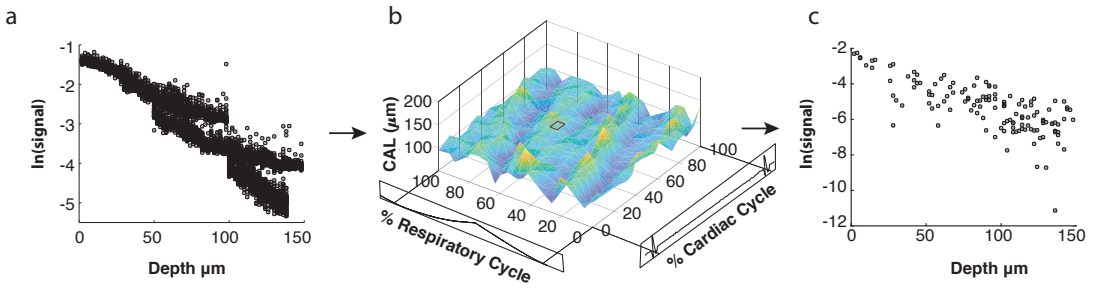

Figure 19. Depth-dependent intensity is used to estimate CAL in three power-adjusted stacks with 50 μm of axial overlap in sequential stack in one mouse. Ungated fluorescence signal attenuation in myocardial tissue shows varied slopes as a function of depth, requiring registration of pixels to specific cardiorespiratory phase before quantification. Restricting data to a subset of cardiorespiratory phase aligns signal attenuation curves allowing for in vivo quantification of the CAL in the beating heart of a respiring animal. a. Raw data of fluorescence from FITC-dextran that labels blood plasma using 1300 nm excitation from three sequential stacks with an overlap of half of the total depth of each stack with the next. Power was adjusted for each stack, with misalignment appearing at the end of the stack. b. Measurement of CAL as a function of cardiorespiratory phase. Data was binned at 5% of both cardiac and respiratory cycles, where each cycle was normalized per beat/breath to set binning restriction. c. Signal attenuation occurring within the 5% x 5% cardiorespiratory phase outlined in the red box in c without apparent misalignment of attenuated signal between stacks.

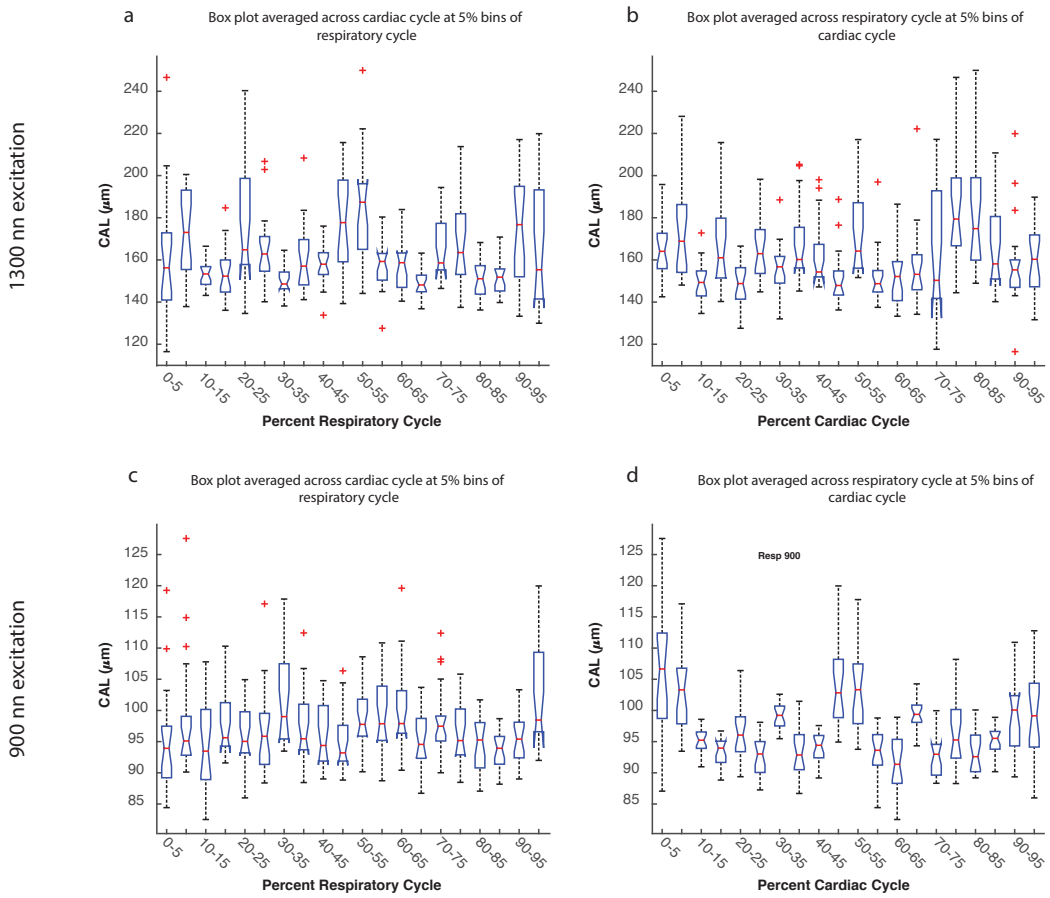

Figure 20. Variability of signal attenuation restricted to a specific phase in cardiorespiratory cycle within myocardium. a. Characteristic attenuation length of 1300 nm signal using 3PE restricted to (a) 5% of the respiratory cycle and averaged across the cardiac cycle in 5% bins and (b) 5% of the cardiac cycle. Characteristic attenuation length of 900 nm signal using 2PE restricted to (c) 5% of the respiratory cycle and averaged across the cardiac cycle in 5% bins and (d) 5% of the cardiac cycle. Red stars on the graph are statistical outliers, whiskers indicate plus minus standard deviation, and box top and the bottom edges of the box represent the 75th percentile of the data

4.4 Discussion

Compared to two-photon excitation with Ti:Sapph laser wavelengths, we demonstrated increased CAL using 1300 and 1700 nm excitation using 3PE, enabling greater imaging depths within the beating heart of a respiring mouse. In brain, CAL has been extensively quantified throughout the wavelengths available for multiphoton

microscopy and shown to be; 131 μm at 775 nm (Kobat et al., 2009), 200 μm at 830 nm (Shih et al., 2012), 285 μm at 1280 nm (Kobat et al., 2009), and at a maximum of 365 μm within the neocortex at 1700 nm (Horton et al., 2013). At both 1280 nm and 1700 nm excitation, the CAL measured in brain are 1.8 times larger than what we report in heart, indicating that in vivo cardiac tissue shows a similar trend of increasing CAL when using excitation wavelengths further into the NIR. The heart is substantially more attenuating than brain. The least amount of attenuation resulted from 1700 nm excitation. This indicates that multiphoton microscopy in the heart stands to gain the same benefit from laser technology for high intensity sources at longer wavelengths as the brain.

One limitation unique to heart is in frame contractile motion that causes image distortion when scanning is less than the velocity of the tissue. The NOPA used here for 3PE was operating at 1 MHz, limiting the pixel dwell time and hence maximum scan rate. We found that even when scanning at 7 fps with a pixel resolution of ~1.5 pixels per μm, which puts the dwell time per pixel at 500 ns and guarantees at least one pulse per pixel, contractile image artifact was still present. Decreasing pixel resolution could mitigate this problem, but this can compromise spatial resolution, which may not be acceptable for all applications. Recently, it was shown that quantification of calcium spikes in the beating heart could be performed with the level of down sampling compatible with fast scanning using low rep rate sources (Jones et al., 2018). If only structural imaging is required, gating for diastole, when cardiac movement is most stable, provides a window for scanning using rates as slow as 1 fps, and if heart stimulation is possible, prospective sequential segmented microscopy can greatly reduce image acquisition time (Vinegoni, Aguirre, Lee, & Weissleder, 2015).

The variability of the clear aperture, arising from the non-uniformity of the attachment of the heart to the cover glass of the stabilization probe during the surgical

procedure, and the intra- and inter-animal variability in the decay curves indicate that more animals are needed. Nonlinear trends present in un-gated decay curves are likely from the motion of the tissue with the cardiorespiratory cycle that results in measurements through different parts of the tissue and improved alignment is required to better quantify trends in the plots of attenuation of signal as a function of depth. Higher speed scanning is helpful for an accurate measure of attenuation. There is a limitation with lower speed scanning for use in cardiac dependent analysis. Slower scanning is not well suited to impose cardiorespiratory gating criteria because the low temporal resolution does not populate every cardiorespiratory phase.

Cyclic fluorescent intensity fluctuations are apparent in free running movies of raw data presumably due to out of plane motion. We have shown previously that on average, systolic contraction moves the tissue toward the surface, which would cause an average increase in intensity. The motion is likely due to the local displacement from the 20% change in ejection fraction of microvessels (Toyota, 2002) rather than myocyte thickening since the aggregate effect of vessel compression would be larger in magnitude than that of myocyte thickening. This systolic movement occurs for a smaller fraction of the heart cycle than diastole so that any brightness associated with tissue movement toward the surface would make the intensity dimmer, on average, since a given fluorescent structure is residing in a deeper point in the tissue. This could help to explain why ungated CAL measurements are consistently lower than gated, however further data is needed to verify this result.

Surprisingly, CAL taken from animals at one-week following cryoinfarction showed similar attenuation curves in animals expressing GFP in Cx3Cr1 positive cells to provide additional sources of fluorescent signal in the regions which have limited vasculature (but still present within the region used for CAL quantification) due to the injury. Varying degrees of fibrosis have been shown in this model that lead to

quantitative differences in scattering (Krishnaswamy et al., 2009). The distinct cell populations which lead to remodeling and repair following injury is a continual topic of research but is known to involve a variety of cell populations especially inflammatory cells.

Here we show that signal intensity variation arising from complex cardiorespiratory motion can be managed through high spatiotemporal resolution scanning and alignment to physiologic signals. We find that 1300 and 1700 nm excitation provides an imaging window, which increases depth of imaging to include many layers of cardiomyocytes in healthy and infarcted tissue in vivo. This increased imaging depth opens up the possibility of further studies to investigate dynamics within the microvessel branches of the coronary arteries buried within the heart wall.

REFERENCES

Aguirre, A. D., Vinegoni, C., Sebas, M., & Weissleder, R. (2014). Intravital imaging of cardiac function at the single-cell level. *Proc Natl Acad Sci U S A, 111*(31), 11257-11262. doi:10.1073/pnas.1401316111

Hatzistergos, K. E., Saur, D., Seidler, B., Balkan, W., Breton, M., Valasaki, K., . . . Hare, J. M. (2016). Stimulatory Effects of Mesenchymal Stem Cells on cKit+ Cardiac Stem Cells Are Mediated by SDF1/CXCR4 and SCF/cKit Signaling Pathways. *Circ Res, 119*(8), 921-930. doi:10.1161/CIRCRESAHA.116.309281

Horton, N. G., Wang, K., Kobat, D., Clark, C. G., Wise, F. W., Schaffer, C. B., & Xu, C. (2013). In vivo three-photon microscopy of subcortical structures within an intact mouse brain. *Nat Photonics, 7*(3). doi:10.1038/nphoton.2012.336

Horton, N. G., & Xu, C. (2015). Dispersion compensation in three-photon fluorescence microscopy at 1,700 nm. *Biomed Opt Express, 6*(4), 1392-1397. doi:10.1364/BOE.6.001392

Jones, J. S., Small, D. M., & Nishimura, N. (2018). In Vivo Calcium Imaging of Cardiomyocytes in the Beating Mouse Heart With Multiphoton Microscopy. *Frontiers in Physiology, 9*(969). doi:10.3389/fphys.2018.00969

Jung, S., Aliberti, J., Graemmel, P., Sunshine, M. J., Kreutzberg, G. W., Sher, A., Littman, D. R. (2000). Analysis of Fractalkine Receptor CX3CR1 Function by Targeted Deletion and Green Fluorescent Protein

Reporter Gene Insertion. *MOLECULAR AND CELLULAR BIOLOGY,, 20*(11), 4106-4114.

Kobat, D., Durst, M. E., Nishimura, N., Wong, A. W., Schaffer, C. B., & Xu, C. (2009). Deep tissue multiphoton microscopy using longer

wavelength excitation. *OPTICS EXPRESS, 17*(16). doi:https://doi.org/10.1364/OE.17.013354

Krishnaswamy, V., Hoopes, P. J., Samkoe, K. S., O'Hara, J. A., Hasan, T., & Pogue, B. W. (2009). *Quantitative imaging of scattering changes associated with epithelial proliferation, necrosis, and fibrosis in tumors using microsampling reflectance spectroscopy*.

Lee, S., Vinegoni, C., Feruglio, P. F., Fexon, L., Gorbatov, R., Pivoravov, M., . . . Weissleder, R. (2012). Real-time in vivo imaging of the beating mouse heart at microscopic resolution. *Nat Commun, 3*, 1054. doi:10.1038/ncomms2060

Li, W., Nava, R. G., Bribriesco, A. C., Zinselmeyer, B. H., Spahn, J. H., Gelman, A. E., . . . Kreisel, D. (2012). Intravital 2-photon imaging of leukocyte trafficking in beating heart. *J Clin Invest, 122*(7), 2499-2508. doi:10.1172/JCI62970

Ouzounov, D. G., Wang, T., Wang, M., Feng, D. D., Horton, N. G., Cruz-Hernandez, J. C., . . . Xu, C. (2017). In vivo three-photon imaging of activity of GCaMP6-labeled neurons deep in intact mouse brain. *Nat Methods, 14*(4), 388-390. doi:10.1038/nmeth.4183

Pologruto, T. A., Sabatini, B. L., & Svoboda, K. (2003). ScanImage: flexible software for operating laser scanning microscopes. *Biomed Eng Online, 2*, 13. doi:10.1186/1475-925X-2-13

Pries, A. R., & Reglin, B. (2017). Coronary microcirculatory pathophysiology: can we afford it to remain a black box? *Eur Heart J, 38*(7), 478-488. doi:10.1093/eurheartj/ehv760

Saederup, N., Cardona, A. E., Croft, K., Mizutani, M., Cotleur, A. C., Tsou, C. L., . . . Charo, I. F. (2010). Selective chemokine receptor usage by central nervous system myeloid cells in CCR2-red fluorescent protein knock-in mice. *PLoS One, 5*(10), e13693. doi:10.1371/journal.pone.0013693

Shih, A. Y., Driscoll, J. D., Drew, P. J., Nishimura, N., Schaffer, C. B., & Kleinfeld, D. (2012). Two-photon microscopy as a tool to study blood flow and neurovascular coupling in the rodent brain. *J Cereb Blood Flow Metab, 32*(7), 1277-1309. doi:10.1038/jcbfm.2011.196

Toyota, E., Fujimoto, K., Kajita, T., Shigeto, F., Matsumoto, T., Goto, M., Kajiya, F. (2002). Dynamic Changes in Three-Dimensional Architecture and Vascular Volume of Transmural Coronary Microvasculature Between Diastolic- and Systolic-Arrested Rat Hearts. *Circulation, 105*, 621-626. doi:https://doi.org/10.1161/hc0502.102964

Vinegoni, C., Aguirre, A. D., Lee, S., & Weissleder, R. (2015). Imaging the beating heart in the mouse using intravital microscopy techniques. *Nat Protoc, 10*(11), 1802-1819. doi:10.1038/nprot.2015.119

CHAPTER 5

CONCLUSIONS AND FUTURE DIRECTION

Advances in laser technology driven by recent influx of funding supporting research aimed at gaining a more fundamental understanding of the brain have pushed once complicated imaging systems into a regime manageable by labs with less of a focus in nonlinear optics. This has already profoundly impacted the neuroscience community by allowing groups to push the breadth of their research questions to limits which were previously unachievable (Ouzounov et al., 2017). Fortunately for the cardiovascular community, they can capitalize on the advancements in imaging made in the neuroscience community over the last decade and will be able to utilize the full power of the most recent research tools available, allowing the potential for ground breaking discovery. Here we have taken some first steps in showing the power and utility of this technology and reported a potentially interesting clinical application after only a brief investigation using these exciting new laser systems. In additional to laser technology, the capability for volumetric imaging at high frame rate using resonant scanning was done on commercially available software that is now available in turn key systems, making this technology more fully accessible to the broader cardiac biology and physiology community.

The use of point tracking to quantify motion trajectories during heart function is not new, for example, the use of radiopaque labels to infer underlying sarcomere function within localized regions has been demonstrated by (Rodriguez, 1992). Studies aimed to better understand the distribution of forces throughout the heart used similar methods to isolated strain through distinct layers of the myocardium to unravel coordinated mechanical mechanisms facilitating efficient pumping (Rodriguez, 1992). However, the tracking performed here is unique in that we can isolate fluorescently

labeled biological structures, such as capillaries, at any point that is accessible within the myocardium. This allows us to establish highly specific motion profiles that are more continuously distributed throughout the tissue, due to high density of distinct capillary structures, opening the potential to establish more complete profiles of layer-specific coordination during contraction. Active motion correction techniques successfully applied to other organs like the spinal cord (Laffray et al., 2011), used optimization algorithms to maintain a constant distance between the objective and the surface of the tissue using reflected light from surface of this tissue. This methodology is not well suited to deal with cardiac motion because of the highly varying, region dependent strain, which changes as a function of depth. Optical sectioning and 3D volume reconstruction as described in Chapter 4 allow the measurement of nearly continuous sections of tissue with micrometer axial resolution to provide accurate tracking of 3D displacement of motion trajectories confined to individual cells.

Here we have shown data averaged over multiple beats, aligned to the R-wave, however, characterization of abnormal calcium activity requires the consideration of beat-to-beat variability. Recently it was shown that macrophages are electrically coupled (Hulsmans et al., 2017), and modulate local activity within the heart. In order to develop a mechanistic understanding of the pathophysiology leading towards fibrillation, arrhythmia, and heart failure following infarction it is clear that the consideration of transient responders such as the macrophages need to be take into consideration to provide a more complete picture of the dynamics at play in the local microenvironment. Point tracking using capillary bifurcation or other fluorescent structures occurring throughout the tissue provides a signal that allows the isolation of this motion unique occurring within a specific cellular region. This sets up an opportunity to use this signal for active feedback correction. Generation of a

waveform that is informed by the axial component of this motion trajectory can then be used to modulate the focus using some type of optical actuation that moves the axial position of the focus to follow the movement of the tissue. Alignment of the waveform to the cardiac cycle has the potential to allow for continuous optical sectioning of individual cells and capillary level vasculature. By reducing the out of plane motion, real time, continuous imaging of individual cells deep within distinct layers of the myocardium, along with the local perfusion of the capillaries surrounding those cells, which has so far not been possible could become practical. Once the axial displacement has been reduced to lateral motion, a sufficiently large enough frame can be used to register locations of capillaries and aligned using a transformation. Once this is done, the data should be well suited to apply methods such as image cross-correlation spectroscopy to measure motion (Wiseman, 2000).

We have demonstrated that even with a high degree of temporal averaging with sufficiently fast spatiotemporal sampling, high precision, quantitative data can be generated using calcium imaging within the beating heart. We have observed that even small, localized damage can result in asynchronous firing throughout the ventricle wall. Without the use of optical sectioning enabled by multiphoton microscopy this observation would not have been possible due to the inability of one photon imaging to isolate contributions from cells beyond the surface. Other groups have shown that there is complex cellular behavior associated with Fstl1 signaling observed in vivo. This protein has been shown to facilitate cardiomyocyte recruitment post injury only when delivered slowly over time on the surface of the epicardium (Wei et al., 2015). Studies such as this further emphasizes the need to develop a more complete picture of dynamic cellular response occurring in vivo with methods capable of resolving depth specific chemical and electrical (Hulsmans et al., 2017) signaling. Additionally, more sophisticated indicators with increased dynamic range and faster

kinetics will allow to more accurately differentiating subtle changes associated with the onset of pathophysiology brought about by injury. GCaMP6f used here has a $t_{1/2\,(off)}$ time of 288 ms, meaning that our measured decay is overestimated, however, newer indicators have improved this dramatically with GCaMP6f$_u$ providing a $t_{1/2\,(off)}$ of 7.8 ms (Helassa, Podor, Fine, & Torok, 2016).

The GCaMP analysis presented here was restricted to the first 100 μm of tissue, and while it is possible to image up to depths of ~250 μm within beating heart tissue using two photon excitation, the background signal quickly goes up beyond 100 μm and the resolution is severely hindered due to wavefront distortion and other factors imposed by the tissue. We have shown here that in vivo myocardial tissue show similar attenuation properties to brain in that it is less attenuating further into the NIR. We also observe that the SNR remains much higher throughout the depth of imaging achievable when using 3PE compared to 2PE. One limiting factor imposed by current technological limitations is that 3PE sources run at a lower repetition rate, limiting the scanning speed so that recording pixel rate does not surpass the rate of pulses put out from the laser. Using galvanometric scanning and averaging over areas much larger than the optical resolution of the imaging system can provide an imaging speed of 15 fps. We found that at 7 fps where, with our system, the dwell time on each pixel is 500 ns, there is still some blurring present within one frame of the image. This indicates that resolving dynamics throughout systole is not possible when using a 1 MHz laser repetition rate, limiting the potential for direct application of our cardiac dynamic imaging approach using this scanning technique with slower sources. It should be noted however that images taken at 7 fps were *nearly* artifact free, leaving a large window for diastolic gating, which is suitable for structural imaging. We have demonstrated that a large level of down-sampling is acceptable when visualizing calcium transients, meaning longer sampling times required to ensure sufficient pulse

delivery can be applied when looking at cellular resolution calcium. There is however a compromise with spatial resolution when down-sampling which is limiting when quantifying other cardiac dependent physiology varying within the cellular microenvironment. For instance, when using an 8-kHz resonant scanner and assuming square pixels, setting a sufficiently long recording time per pixel for a laser repetition rate of 1MHz requires pixel binning of 32x32 pixels per line resulting in a 16x16 pixel image to have just one pulse per pixel. Increasing the repetition rate to 4 MHz puts the pixel size required for at least one pulse per pixel at 128x128 pixel frames, with 1.4 pulses on average per pixel. This also pushes the frame rate to 120 fps, which is more ideal for studying cellular beat-to-beat variability such as an inflammatory cell response that is dynamically varying throughout the imaging session. To further increase the SNR a 4 kHz resonant scanner would put the average pulses per pixel at 2.8 using a 4 MHz source with a frame rate of 120 fps which may offer a reasonable compromise for sampling in a contracting tissue while still using high pulse energy, low rep rate source. If imaging is not necessary but a high temporal sampling is desired across the cardiorespiratory cycle then limiting the analysis to exclude regions which were acquired with no laser pulse using a intensity percentile restriction may be used. This will allow for adequate spatial sampling in the cardiorespiratory cycle to apply rigid gating criteria.

We have taken some first steps in using the power of nonlinear microscopy to study cardiovascular disease. We have shown that there are clinically relevant endogenous signals present in plaques, provided methods to isolated cellular scale action potentials in vivo, and investigated the practicality of using further NIR sources, combined with 3PE for use in the beating heart. The incorporation of additional labels, active stabilization methods, and more rigidly controlled injury models hold great promise for future applications of this technology.

REFERENCES

Helassa, N., Podor, B., Fine, A., & Torok, K. (2016). Design and mechanistic insight into ultrafast calcium indicators for monitoring intracellular calcium dynamics. *Sci Rep, 6*, 38276. doi:10.1038/srep38276

Hulsmans, M., Clauss, S., Xiao, L., Aguirre, A. D., King, K. R., Hanley, A., . . . Nahrendorf, M. (2017). Macrophages Facilitate Electrical Conduction in the Heart. *Cell, 169*(3), 510-522 e520. doi:10.1016/j.cell.2017.03.050

Laffray, S., Pages, S., Dufour, H., De Koninck, P., De Koninck, Y., & Cote, D. (2011). Adaptive movement compensation for in vivo imaging of fast cellular dynamics within a moving tissue. *PLoS One, 6*(5), e19928. doi:10.1371/journal.pone.0019928

Ouzounov, D. G., Wang, T., Wang, M., Feng, D. D., Horton, N. G., Cruz-Hernandez, J. C., . . . Xu, C. (2017). In vivo three-photon imaging of activity of GCaMP6-labeled neurons deep in intact mouse brain. *Nat Methods, 14*(4), 388-390. doi:10.1038/nmeth.4183

Rodriguez, E. K., Hunter, W., C., Royce, M. J., Leppo, M. K., Douglas, A. S., Weisman, H. F. (1992). A method to reconstruct myocardial sarcomere lengths and orientations at transmural sites in beating canine heart. *Am J Physiol, 263*(1), H293-306. doi:10.1152/ajpheart.1992.263.1.H293

Wei, K., Serpooshan, V., Hurtado, C., Diez-Cunado, M., Zhao, M., Maruyama, S., . . . Ruiz-Lozano, P. (2015). Epicardial FSTL1 reconstitution regenerates the adult mammalian heart. *Nature, 525*(7570), 479-485. doi:10.1038/nature15372

Wiseman, P. W., Squier, J. A., Ellisman, M. H., Wilson, K. R. . (2000). Two-photon image correlation spectroscopy and image cross-correlation spectroscopy

Journal of Microscopy, 200(1), 14-25. doi:https://doi.org/10.1046/j.1365-2818.2000.00736.x